

A Non Parametric Model for the Cosmic Velocity Field

E. Branchini¹, L. Teodoro¹, C.S. Frenk¹, I. Schmoldt²,
 G. Efstathiou³, S.D.M. White⁴, W. Saunders⁵, W. Sutherland²,
 M. Rowan-Robinson⁶, O. Keeble⁶, H. Tadros⁷, S. Maddox³, S. Oliver⁶,

¹*Department of Physics, University of Durham, South Road, Durham DH1 3LE, UK*

²*Department of Physics, University of Oxford, Keble Road, Oxford OX1 3RH, UK*

³*Institute of Astronomy, University of Cambridge, Madingley Road, Cambridge CB3 0HA, UK*

⁴*Max Planck Institut für Astrophysik, Karl-Schwarzschild-Straße 1, 85740 Garching, Germany*

⁵*Institute for Astronomy, University of Edinburgh, Blackford Hill, Edinburgh EH9 3JS, UK*

⁶*Imperial College of Science, Technology, and Medicine, Blackell Laboratory, Prince Consort Road, London SW1 2EZ, UK*

⁷*Department of Physics, University of Sussex, Falmer, Brighton BN1 9QH, UK*

1 October 2018

ABSTRACT

We present a self-consistent nonparametric model of the local cosmic velocity field derived from the distribution of IRAS galaxies in the PSCz redshift survey. The survey was analyzed using two independent methods, both based on the assumptions of gravitational instability and linear biasing. The two methods, which give very similar results, were tested and calibrated on mock PSCz catalogues constructed from cosmological N-body simulations. The denser sampling provided by the PSCz survey compared to previous IRAS galaxy surveys allows an improved reconstruction of the density and velocity fields out to large distances. The most striking feature of the model velocity field is a coherent large-scale streaming motion along the baseline connecting Perseus–Pisces, the Local Supercluster, the Great Attractor, and the Shapley Concentration. We find no evidence for back-infall onto the Great Attractor. Instead, material behind and around the Great Attractor is inferred to be streaming towards the Shapley Concentration, aided by the compressional push of two large nearby underdensities. The PSCz model velocities compare well with those predicted from the 1.2Jy redshift survey of IRAS galaxies and, perhaps surprisingly, with those predicted from the distribution of Abell/ACO clusters, out to $140 h^{-1}$ Mpc. Comparison of the real-space density fields (or, alternatively, the peculiar velocity fields) inferred from the PSCz and cluster catalogues gives a relative (linear) bias parameter between clusters and IRAS galaxies of $b_c = 4.4 \pm 0.6$. Finally, we implement a likelihood analysis that uses all the available information on peculiar velocities in our local universe to estimate $\beta = \Omega_0^{0.6}/b = 0.6_{-0.15}^{+0.22}$ ($1-\sigma$), where b is the bias parameter for IRAS galaxies.

Key words: Cosmology: theory – galaxies: large-scale structure, large-scale dynamics.

1 INTRODUCTION

The art of modelling the cosmic velocity field, which originates from the desire to interpret observed deviations from a uniform Hubble expansion, has developed rapidly over the past few years. There are two main reasons for this. One is an increase in the quantity and quality of measured galaxy peculiar velocities. The other is the advent of nearly all-sky, flux-limited, redshift surveys that allow self-consistent theoretical predictions to be made with the requisite accuracy.

Although other possibilities have been proposed (e.g. Babul *et al.* 1994), the gravitational instability theory (Peebles 1980) has proven to be the most successful theoretical framework in which to interpret peculiar velocity data in relation to inhomogeneities in the mass distribution. Early attempts to account for observed velocities within this general framework were rather simplistic due to incomplete knowledge of the distribution of galaxies in the local universe. Thus, simple parametric models were developed to describe cosmic flows in terms of infall onto one or more spherical overdensities such as the Virgo Cluster, the Great Attractor or the Perseus Pisces supercluster (Davis and Peebles 1983, Lynden-Bell *et al.* 1987, Peebles 1988, Han and Mould 1990). The situation changed dramatically when statistically complete, nearly all-sky, redshift catalogues of galaxies were constructed since it then became possible to predict peculiar velocities directly, assuming that luminous objects trace the underlying density field in some fashion. Since then, several modelling procedures have been developed which are generally based on the simplifying assumption that the gravitating mass is distributed just like the tracer objects (galaxies or clusters), although the relative amplitude of the deviations from uniformity, usually called the bias, is taken to be a free parameter. In addition to this “linear bias model,” current methods also assume gravitational instability in the linear or mildly nonlinear regime (e.g. Yahil *et al.* 1991, Kaiser *et al.* 1991, Nusser and Davis 1994, Fisher *et al.* 1995b, Sigad *et al.* 1998), and so require smoothing over scales where non-linear effects are important. This necessitates the additional assumption that smoothing a distribution that has evolved to a nonlinear state gives a result that can be modeled by linear or quasilinear evolution from smoothed initial conditions.

Because of their large sky coverage, the most extensively used redshift surveys are those based on the “Point Source Catalogue” (PSC) of IRAS galaxies (e.g. the 1.9 Jy survey of Strauss *et al.* 1990, the upgraded 1.2 Jy catalogue of Fisher *et al.* 1995a, or the deeper but sparser QDOT survey of Rowan-Robinson *et al.* 1990). Other catalogues containing different kinds of objects such as optically selected galaxies (e.g. Shaya, Tully and Pierce 1990, Hudson 1994, Baker *et al.* 1998) or clusters of galaxies (Scaramella 1995 Branchini and Plionis 1996) have also been used to produce model velocity fields on scales up to $200 h^{-1} \text{Mpc}^*$.

Comparison of a model velocity field with directly measured peculiar velocities provides a means to constrain the density parameter, Ω_0 , while also testing the gravitational instability hypothesis and the assumed biasing scheme. A successful model for the peculiar velocity field may be used to recover the distribution of galaxies or clusters in real space, directly from their measured redshifts. This, in turn, allows investigation of the statistical properties of the objects’ distribution, free from the effects of redshift space distortions. Overall, model velocity fields constructed using different surveys have proved to be remarkably consistent with one another (Freudling, da Costa and Pellegrini 1994, Baker *et al.* 1998) and have succeeded in reproducing most of the characteristics exhibited by maps made directly from observed peculiar velocities. There are, however, two notable exceptions: the large bulk motion on very large scales claimed by Lauer and Postman (1994) and a dipolar coherence in the residuals between the velocity field obtained from the Mark III catalogue (Willick *et al.* 1997) and the IRAS 1.2Jy gravity field on scales of $\sim 50 h^{-1} \text{Mpc}$ (Davis, Nusser and Willick 1996).

Here we present a new nonparametric model of the cosmic velocity field based on the recently completed PSCz survey of IRAS galaxies. This is the last of the nearly all-sky redshift surveys based on the IRAS catalogue and supersedes both the 1.2Jy and the QDOT catalogues which it contains. The denser sampling and lower flux limit of the PSCz survey allows us to model the peculiar velocity field on larger scales than was possible before without excessive contamination from shot noise.

* Throughout this paper we write Hubble’s constant as $H_0 = 100h \text{ km s}^{-1} \text{ Mpc}^{-1}$

The outline of this paper is as follows. In §2 we describe the PSCz dataset as well as two other redshift catalogues that we use to construct independent model velocity fields. Two methods for generating the PSCz peculiar velocity fields have been implemented in order to keep track of systematic errors. These are presented in §3, together with a detailed error analysis. A cosmographic tour is performed in §4, along with a consistency check between the two PSCz velocity models and a comparison between the PSCz and 1.2Jy model velocity fields. In §5 we take advantage of the large depth of the PSCz survey to compare the gravity field derived from it with the one derived from the distribution of Abell/ACO clusters. An estimate of the parameter $\beta \simeq \Omega_0^{0.6}/b$, where b is the linear bias parameter of IRAS galaxies, is obtained in §6 by comparing observed and predicted bulk velocity vectors. In §7 we discuss our results further and summarise our main conclusions.

2 THE DATASETS

The main dataset used in this work is the recently completed PSCz redshift survey described in detail by Saunders *et al.* (1998a). The catalogue contains some 15,500 IRAS PSC galaxies with 60 μm flux, $f_{60} > 0.6$. The construction of the catalogue is described in detail in Saunders *et al.* (1998a) and so we only summarize here its main features. The selection of potential galaxies from the PSC emphasised completeness at the expense of contamination by cirrus, stars, AGN, etc. Because the completeness of the PSC is not guaranteed to 0.6Jy in 2HCON areas (Beichman *et al.* 1988, PSC explanatory supplement), we added to the PSC any 1HCON detections from the Point Source Catalogue Reject file with FSS counterparts (Moshir *et al.* 1989). We then selected sources with $f_{100} < 4f_{60}$ (to eliminate the vast majority of cirrus sources) and $f_{60} > 0.5f_{25}$ (to eliminate the vast majority of stars). Residual contamination was eliminated by a combination of optical identification on Schmidt plates, examination of the raw IRAS addscan profile, information from the Simbad database and, where still unclear, optical spectroscopy. Large galaxies can have their flux underestimated by the IRAS beam, so we constructed an all-sky list of optically-selected galaxies with extinction-corrected diameters larger than 2.25'. The PSC detections for these galaxies were flagged for deletion. The optical catalogue was addscanned by IPAC, and we used software provided by Amos Yahil to derive fluxes from the addscan profiles, and where the flux was sufficient, added them to the catalogue.

For our purposes, one of the most important properties of the PSCz catalogue is its large sky coverage. The only excluded regions are two thin strips in ecliptic longitude that were not observed by IRAS, the Magellanic clouds, and the area in the galactic plane where the B-band extinction, A_B , exceeds 2 magnitudes. The extinction is estimated from the 100 μm background, and includes a correction for the estimated temperature gradient in the Milky Way (Saunders *et al.* 1998a). Overall, the PSCz catalogue covers $\sim 84\%$ of the sky. Although we will occasionally consider galaxies with recession velocity as large as 30000 km s^{-1} , for the most part we will restrict our analysis to the PSCz subsample of 11206 galaxies within 20000 km s^{-1} in the Local Group (LG) frame. The distribution on the sky of PSCz galaxies is shown in galactic coordinates (Aitoff projection) in the upper part of Fig. 1.

For comparison purposes, we have also applied our analysis to the similar, but shallower, IRAS 1.2Jy redshift survey (Fisher *et al.* 1995a). Galaxies in this catalogue were also selected from the IRAS PSC but using a higher (ADDscan) flux limit, $f_{60} > 1.2$ Jy, and different criteria for minimizing contamination by galactic cirrus. This catalogue has a somewhat larger sky coverage of $\sim 88\%$. Here we will use the 4939 IRAS 1.2 Jy galaxies within 20000 km s^{-1} of the Local Group.

Finally, in an attempt to extend our analysis, we use a completely different set of mass tracers consisting of a volume-limited sample of optically-selected galaxy clusters extracted from the Abell (1958) and the Abell, Corwin & Olowin (1989; hereafter ACO) catalogues. These were combined into a single homogeneous catalogue using the clusters in common between the two samples, according to the prescription described by Branchini and Plionis (1996; hereafter BP96). The sample has a limiting depth of 250 h^{-1} Mpc and contains 493 clusters of richness class $R \geq 0$ at $|b| \geq 13^\circ$, and $m_{10} < 17$, where m_{10} is the magnitude of the tenth brightest galaxy in the cluster.

The number of galaxies in a flux limited sample decreases with distance, as may be seen in the lower plot of Fig. 2, for the PSCz (upper histogram) and 1.2 Jy (lower, shaded histogram) surveys. We define a selection function,

$\phi(r)$, as the fraction of galaxies that can be seen out to a redshift distance $r = \frac{cz}{H_0}$ (expressed in h^{-1} Mpc), given the survey flux limit. To determine $\phi(r)$ we use the parametric maximum likelihood estimate proposed by Yahil *et al.* (1991), in which the following analytic form for the selection function is assumed:

$$\phi(r) = Ar^{-2\alpha} \left(\frac{1+r^2}{r_*^2} \right)^{-\beta} \quad \text{if } r > r_s. \quad (1)$$

The value of the normalization constant, A , does not affect the modeling of peculiar velocities. In this paper we arbitrarily set $\phi(r) = 1$ if $r \leq r_s$ with $r_s = 6 h^{-1}$ Mpc. This choice is equivalent to imposing a lower cutoff in the $60 \mu m$ luminosity which, in turn, avoids giving too much weight to faint, nearby IRAS galaxies that may not trace the galaxy distribution reliably in the nearby volume (Rowan Robinson *et al.* 1990). The relevant parameters have been determined via likelihood analysis using only the objects within $100 h^{-1}$ Mpc. The results are displayed in Table 1 for the PSCz and 1.2Jy surveys, both in redshift (z -) and real (R-) space (i.e. after correction for redshift space distortions as discussed in §3.1). The number density of galaxies as a function of redshift distance, predicted by eqn. (1), is shown in the lower part of Fig. 2, superimposed on the observed $N(r)$ histograms. The theoretical curves provide a good description of the data. The ratio of the number of observed to the number of expected galaxies gives the radial overdensity field, shown in the upper part of Figure 2 for both the PSCz (thick line) and the IRAS 1.2Jy catalogues. A horizontal line is drawn at the mean density. The radial density fields traced by the two surveys are consistent with one another, but the larger shot noise in the 1.2 Jy sample makes the amplitude of density fluctuations larger than in the PSCz survey at large radii.

Our estimator for the selection function is independent of clustering but requires prior knowledge of the evolutionary rate. Springel and White (1998) have recently developed a new technique to estimate the rate of evolution of the selection function. For the 1.2Jy catalogue they find rather strong evolution and this is even more dramatic in the PSCz catalogue (Springel 1996). Ignoring this effect could introduce spurious streaming motions in the model velocity field. However, we have verified that our selection function for PSCz is very similar to the one derived by Springel (1996) within the scales relevant to our analysis. The difference between the two selection functions increases with distance but it is only 5% at $200 h^{-1}$ Mpc. Strong evolutionary effects become important only beyond these scales and we shall therefore ignore them in our modeling.

For the Abell/ACO composite sample we adopt the selection function derived by BP96:

$$\phi(r) = \begin{cases} 1 & \text{if } r \leq r_{c1} \\ 0.5(1 + A_1 \exp(-r/r_{o1})) & \text{if } r_{c1} < r \leq r_{c2} \\ 0.5(A_2 \exp(-r/r_{o2}) + A_1 \exp(-r/r_{o1})) & \text{if } r > r_{c2} \end{cases} \quad (2)$$

The estimated values of the parameters are listed in Table 2, and the expected number of clusters as a function of redshift distance is shown in the lower plot of Fig. 2 as a thick line.

The mean separation, l , of the objects in a population of tracers limits the intrinsic resolution with which we the population probes the underlying cosmic fields. Thus, $R_s = l$, is a natural smoothing length which keeps the shot noise at a constant level. In a magnitude limited survey, l increases with distance r according to:

$$l(r) = [\phi(r)\langle n \rangle]^{-1/3}, \quad (3)$$

where the average number density of objects $\langle n \rangle$ has been estimated as

$$\langle n \rangle = \frac{1}{V} \sum_{i=1}^{N_g} \phi(r_i)^{-1}, \quad (4)$$

and the sum extends over all N_g objects contained within the volume sampled, V . The value of the average number density within $100 h^{-1}$ Mpc, computed in redshift and real space, is shown in Table 1 both for the PSCz and IRAS 1.2 Jy catalogues. The more physically meaningful values of the mean galaxy separation at $100 h^{-1}$ Mpc, $l(r)$ expressed in $h^3 \text{ Mpc}^{-3}$, are also given in the table. Because of our normalization ($\phi(r) = 1$ within $6 h^{-1}$ Mpc), our estimate of $\langle n \rangle$ for the 1.2 Jy galaxies is slightly different from that of Fisher *et al.* (1995a). Fig. 3 shows the mean interobject separation as a function of r for the three samples considered. Because of the shallower depth of the 1.2Jy sample,

its intergalaxy separation increases much more steeply with distance than in the PSCz sample. Thus, at a fixed resolution, the PSCz survey probes cosmic structures out to larger distances than the 1.2 Jy survey without an increase in shot noise. The dot-dashed line in Fig. 3 shows the Abell/ACO mean intercluster separation. Locally, this is much larger than the corresponding separation in the galaxy surveys, but on scales above $170 h^{-1}$ Mpc, clusters start to become more effective than IRAS 1.2Jy galaxies in tracing the cosmic density fields.

3 NON-PARAMETRIC MODELS OF THE COSMIC VELOCITY FIELD

The main aim of this paper is to obtain a self-consistent, non-parametric model of the velocity field in the local universe (i.e. for $r < 150 h^{-1}$ Mpc). We do this by removing the redshift space distortions that affect the observed radial galaxy distribution in the survey using two different procedures. The first is the iterative technique devised by Strauss & Davis (1988), applied by Yahil *et al.* (1991), and further refined by Sigad *et al.* (1998). The results presented here were obtained by applying the original Yahil *et al.* (1991) technique. The second procedure, used here primarily as a check for possible systematic effects, is the non-iterative technique developed by Nusser and Davis (1994).

3.1 The methods

The two procedures that we have implemented rely on three important assumptions. Firstly, cosmic structures are assumed to have grown by gravitational amplification of small amplitude fluctuations present in the density field at early times (gravitational instability, c.f. Peebles 1980). Secondly, fluctuations on the scales of interest are assumed to be small enough that linear (or mildly non-linear) theory is applicable. Thirdly, luminous objects (galaxies or clusters) are assumed to trace the underlying mass density field according to:

$$\delta_l(\mathbf{r}) = b_l \delta(\mathbf{r}), \quad (5)$$

where δ is the mass overdensity at position \mathbf{r} , δ_l is the fluctuation in the number of luminous objects at this same location, and b_l is the biasing parameter. Eqn. (5) is often referred to as the “linear biasing model.” The reconstruction methods return a model of the cosmic velocity field that depends on the parameter $\beta = \Omega_0^{0.6}/b_l$. The value of β must be determined *a posteriori* by comparison with other observational data.

The two reconstruction techniques that we use are extensively discussed and tested by Branchini *et al.* (1998) where the reader may find further details. Here, we simply outline the main principles of each method.

Method 1: The iterative technique

In linear theory the overdensity is related to the peculiar velocity field by

$$\nabla \cdot \mathbf{v} = -\beta \delta_l. \quad (6)$$

The model velocity field is then obtained by iteratively solving the system of equations:

$$\mathbf{v}(\mathbf{r}) = \frac{H_0 \beta}{4\pi} \int d^3 \mathbf{r}' \frac{\mathbf{r}' - \mathbf{r}}{|\mathbf{r}' - \mathbf{r}|^3} \delta_l(\mathbf{r}') \quad (7)$$

and

$$r = cz - \hat{\mathbf{r}} \cdot (\mathbf{v} - \mathbf{v}_{LG}). \quad (8)$$

Eqn (7) follows from integrating eqn (6); \mathbf{v} is the peculiar velocity of a tracer object at position given by the radial unit vector $\hat{\mathbf{r}}$; and \mathbf{v}_{LG} is the velocity of the Local Group.

During each iteration, the selection function and the mean number density of the population of displaced objects are recomputed. Eqns (6) and (7) are only valid in the linear regime and so the force field needs to be smoothed to eliminate nonlinear effects. We employ a “top hat” filter with a smoothing radius $R_s(r) = \max[5, (\langle n \rangle \phi(r))^{-1/3}] h^{-1}$ Mpc. This choice eliminates most of the nonlinear contributions and keeps the shot noise at a constant level. To improve numerical convergence, we adiabatically increase the value of β at each of ten iterations, from 0.1 to 1.0

(Strauss *et al.* 1992b). Note that the amplitude of the velocity vectors scales, to first order, linearly with β . Unless otherwise stated, all the plots of the model velocity fields that we present assume $\beta = 1$.

Around high density regions, such as clusters, there may be triple-valued regions in which the same redshift is observed at three different positions along a given line-of-sight. We correct for this by collapsing the galaxies within clusters and implementing the “robust procedure” (“method 2”) of Yahil *et al.* (1991) to determine the locations of galaxies within triple-valued regions. For the collapsing procedure, we have used two different datasets: the six nearest clusters listed in Table 2 of Yahil *et al.* (1991) and a larger catalogue of 61 objects obtained by merging the 59 SMAC clusters of Hudson *et al.* (1998) with the Yahil *et al.* (1991) dataset. The results show that the collapsing procedure only affects the infall pattern around rich clusters. However, with the level of smoothing used here, the effect is negligible and no systematic differences are found when the model velocity fields are compared on a point-by-point basis.

Method 2: Spherical harmonics expansion

This procedure is based on the method proposed by Nusser and Davis (1994). In linear theory, the velocity field in redshift space is irrotational and thus may be derived from a velocity potential:

$$\mathbf{v}(\mathbf{s}) = -\nabla\Phi(\mathbf{s}). \quad (9)$$

Expanding the potential and the galaxy density field, δ^g , in spherical harmonics, and using the Zel’dovich approximation, it can be seen that the two fields obey a Poisson-like equation:

$$\frac{1}{s^2} \frac{d}{ds} \left(s^2 \frac{d\Phi_{lm}}{ds} \right) - \frac{1}{1+\beta} \frac{l(l+1)\Phi_{lm}}{s^2} = \frac{\beta}{1+\beta} \left(\delta_{lm}^g - \frac{1}{s} \frac{d \ln \phi}{d \ln s} \frac{d\Phi_{lm}}{ds} \right), \quad (10)$$

where δ_{lm}^g and Φ_{lm} are the spherical harmonic coefficients of the galaxy density and velocity potential fields respectively. We have considered the coefficients up to $l \leq l_{max} = 15$ and $|m| \leq l_{max}$. We employ a Gaussian filter with smoothing radius $R_s(r) = \max[3.2, (\langle n \rangle \phi(r))^{-1/3}] h^{-1}$ Mpc, compute the coefficients δ_{lm}^g in redshift shells for the different catalogues, solve eqn. (10) for Φ_{lm} , and then compute the full three-dimensional velocity field in redshift space using eqn. (9). Galaxy positions and peculiar velocities at the real space positions, \mathbf{r} , are obtained by assuming a one-to-one mapping between the real and redshift space positions, \mathbf{r} and \mathbf{s} , along the line-of-sight. We minimize the problem of triple-valued regions by adopting the same cluster-collapsing scheme used above.

Redshift space distortions are only one of several effects that hamper the recovery of cosmic density and velocity fields from observational data. Incomplete sky coverage is another, potentially serious, problem and we deal with it using a filling method similar to that introduced by Yahil *et al.* (1991). We use their original technique to fill in the region at galactic latitude $|b| \leq 8^\circ$, but each real PSCz galaxy at $|b| \leq 8^\circ$ is included to replace a synthetic object that resides in the same longitude-distance bin. Masked regions at larger galactic latitudes are filled in with a random distribution of synthetic galaxies having the observed mean number density. Tests performed by Branchini *et al.* (1998) using the mock catalogues described in the next section show that the only bias introduced by this filling in technique is a spurious bulk motion of $< 60 \text{ km s}^{-1}$ (see §6.1). As a further check we have also used the new Fourier interpolation technique developed by Saunders *et al.* (1998b), which interpolates structure across the mask under the assumption that the density field of galaxies is a lognormal random field. In doing this, we have used a ‘tapered’, or radially-dependent, mask to take into account the known incompleteness in the PSCz at large distances ($> 15000 \text{ km s}^{-1}$) and low latitudes ($A_B > 1^m$), due to difficulties in making secure identifications and obtaining redshifts for obscured distant galaxies. The area of sky across which we interpolate is defined by $A_B = 2^m$ at $V < 15000 \text{ km s}^{-1}$, increasing to $A_B = 1^m$ at $V = 30000 \text{ km s}^{-1}$. Outside this volume, the PSCz is essentially complete. The model velocities predicted using this mask turned out to be almost identical to the ones obtained using the simpler filling in procedure described above.

Another source of random and systematic error is the radial selection function which, when coupled to redshift distortions, generates the so called ‘rocket effect’ discussed by Kaiser and Lahav (1989). This is a spurious acceleration measured from a magnitude-limited sample of galaxies by an observer who has a peculiar velocity unrelated to the true gravitational acceleration. In Method 1 this effect is quantified and corrected for using the mock catalogues

discussed below. In Method 2 the rocket effect is explicitly accounted for by the second term in the right-hand side of eqn. (10).

Finally, another potential source of bias is the fact that IRAS galaxies are preferentially of late morphological type and are less clustered than early types (Strauss *et al.* 1992a, Hermit *et al.* 1996). However, any biases arising from this are likely to be small since Baker *et al.* (1998) have shown that the ratio of the amplitudes of IRAS and optical galaxy density fields, smoothed on scales $\geq 5 h^{-1}$ Mpc, is almost constant, implying a ratio of linear biasing parameters of $b_o/b_I \simeq 1.4$.

3.2 Error estimates using mock catalogues

We have used a suite of large cosmological N-body simulations to generate mock galaxy catalogues that mimic the main properties of the PSCz and 1.2Jy redshift surveys. We use these to quantify random and systematic errors in our reconstructed velocity fields. For the fields inferred from cluster catalogues, we adopt the error estimates derived by BP96 and by Branchini *et al.* (1997) on the basis of a hybrid Monte Carlo/mock catalogue technique.

The simulations we use are those described by Cole *et al.* (1998). We consider two different cold dark matter cosmologies: a flat model with $\Omega_0 = 0.3$ and cosmological constant term, $\Lambda c^2/3H_0^2 = 0.7$, and a critical density universe ($\Omega_0 = 1.0$) with power spectrum shape parameter, $\Gamma = 0.25$. In both cases, the fluctuation amplitude was normalized by the observed abundance of galaxy clusters. This requires setting $\sigma_8 = 0.55\Omega_0^{-0.6}$ (Eke, Cole & Frenk 1996), where σ_8 is the linear rms mass density fluctuation in top hat spheres of radius $8h^{-1}$ Mpc. Galaxies were identified with random particles from the simulations (so that $b = 1$ by construction). Prior to generating the mock catalogues, we smoothed the velocities in the simulations using a top hat filter of radius $1.5 h^{-1}$ Mpc. This brings $\sigma_{12}(1)$, the pairwise velocity dispersion of objects with projected separation $\leq 1 h^{-1}$ Mpc, down to ~ 250 km s $^{-1}$ (when only particles within $30 h^{-1}$ Mpc from the observer are considered). This value is in accordance with the recent analysis of the Optical Redshift Survey of Santiago *et al.* (1995, 1996) by Strauss, Ostriker and Cen (1998) for galaxies outside high density regions. and with the estimate of $\sigma_{12}(1)$ for late type galaxies in the Perseus–Pisces redshift catalogue by Guzzo *et al.* (1997). Both these measurements refer to ‘field’ galaxies, and are therefore well matched to the late type IRAS galaxies of the PSCz catalogue.

Each mock PSCz catalogue is contained in a sphere of radius $170 h^{-1}$ Mpc and, for the purposes of error analyses, 10 nearly independent mock catalogues were obtained from each cosmological model. Several constraints were applied in order to obtain mass distributions and velocity fields as similar as possible to those observed:

- 1) Local Group observers. Hypothetical observers were selected from the set of particles with velocity, $\mathbf{v}_{LG} = 625 \pm 25$ km s $^{-1}$, lying in regions in which the shear within $5 h^{-1}$ Mpc is smaller than 200 km s $^{-1}$ and the fractional overdensity within the same scale ranges between -0.2 and 1.0 (Brown and Peebles 1987). These constraints mimic the Local Group environment.
- 2) Coherent galaxy dipole. A galactic coordinate system, (l, b) , in the (periodic) computational volume was defined such that the velocity of the observer pointed towards $(l, b) = (276, 30)$, the direction of the dipole anisotropy observed in the cosmic microwave background (CMB) radiation. This dipole is known to be approximately aligned with the dipole in the distribution of IRAS galaxies (Strauss *et al.* 1992a, Schmoldt *et al.* 1998).
- 3) Radial selection. We generated flux–limited “galaxy” samples using a Monte Carlo rejection procedure to select particles in the simulations, assigning them fluxes according to eqn. (1). In the vicinity of an observer, the particle number density in the simulation is less than the number density of galaxies in the PSCz and 1.2Jy catalogues. We therefore generated catalogues that are semi–volume limited at a radius of $10.9 h^{-1}$ Mpc for PSCz and $7.8 h^{-1}$ Mpc for 1.2Jy.
- 4) Masked areas. To mimic the incomplete sky coverage, we excluded all objects within the unobserved regions in the two IRAS catalogues.

The distribution on the sky of the galaxies in one of our PSCz mock catalogues is shown, as an Aitoff projection, in the lower panel of Fig. 1, where it may be compared to the real survey displayed in the upper panel. An illustration of the utility of these mock catalogues is provided in Fig. 4. The upper left–hand panel displays a two dimensional slice,

corresponding to the mock Supergalactic plane, through the density and velocity fields within a region of $120 h^{-1}$ Mpc. Both fields were tabulated on a 64^3 grid and subsequently smoothed using a Gaussian filter with a constant effective radius of $6 h^{-1}$ Mpc. The upper right-hand panel shows density and velocity fields reconstructed using Method 1. All the main features, as well as most of the small scales structure, are correctly reproduced. The agreement between the fields can be better appreciated from the two lower plots. The one on the left shows the absolute value of the errors in the reconstructed density field. The main discrepancies occur within the zone-of-avoidance, depicted as a shaded region, and at large distances where the shot noise is large. A correlation between the error and the signal is present only in the outer regions. The lower right-hand plot displays the differences between the two velocity vector fields. Again, the largest discrepancies occur at large distances and no strong coherence is detected. Very similar results are obtained when the reconstruction is performed using Method 2.

Unless otherwise stated, the same Gaussian filter of $6 h^{-1}$ Mpc is used throughout the rest of this paper. As discussed in §2, a smoothing radius of $6 h^{-1}$ Mpc corresponds to the average galaxy separation at $\sim 80 h^{-1}$ Mpc, i.e. to the maximum distance out to which comparisons with observed peculiar velocities are still possible. The drawback of using a constant smoothing is that the shot noise increases with distance, artificially enhancing the density contrast in the outer regions, as may be seen in Fig. 4. With our adopted smoothing, the average shot noise in $\delta(\mathbf{r})$ at a distance of $80 h^{-1}$ Mpc is $\sim 96\%$, rapidly increasing to $\sim 180\%$ at $120 h^{-1}$ Mpc. A complete description of the mock catalogues, their use for error estimation and a detailed assessment of the reliability of our galaxy reconstruction methods is given in Branchini *et al.* (1998). The corresponding analysis for the Abell/ACO cluster catalogues may be found in Branchini *et al.* (1997).

4 A COSMOGRAPHIC TOUR

In this Section we present a qualitative description of the model density and velocity fields of the local universe derived from the PSCz survey. We analyse the data using Method 1 above. Visualizing three dimensional structures and the corresponding vector fields, is not easy. Fortunately from this point of view, the most interesting structures in the nearby universe, on scales larger than the Local Supercluster, are roughly distributed along a planar structure, de Vaucouleurs' (1953) Supergalactic plane (at Supergalactic coordinates $SGZ=0$). In this analysis we will mainly follow the custom of displaying the density and velocity features in a two dimensional slice through this plane. However, distributions along other parallel planes will also be displayed.

With the depth and sampling frequency of the PSCz survey, a reliable map of the density field can be constructed out to a distance of $150 h^{-1}$ Mpc. Fig. 5 shows a slice through the Supergalactic plane of an *adaptively smoothed* overdensity field. Within $30 h^{-1}$ Mpc a constant Gaussian filter of radius $3 h^{-1}$ Mpc was used, but beyond that the radius of the filter increases linearly with distance up to $11.25 h^{-1}$ Mpc at $150 h^{-1}$ Mpc. This variable smoothing filter was chosen to maintain a roughly constant sampling error over the large range of scales considered. It represents a compromise between resolution in the inner regions and acceptable shot noise errors near the edge. The drawback is that, unlike the case of constant smoothing, the density contrast decreases with distance, as is clear from the map. (The $\delta = 0$ level is indicated by the yellow line.) The most striking feature of this map is the large-scale coherence of the mass distribution. Interconnected overdensities, separated by very large voids, extend over distances of order $100 h^{-1}$ Mpc. The most prominent structure, which plays a major role in the dynamics of the local flow field, is the overdense ridge extending from the Perseus-Pisces supercluster, close to the centre of the map, all the way to the Shapley concentration near the top left corner.

The PSCz survey is large enough that the velocity field corresponding to the mass distribution can be reconstructed quite accurately, with a relative error always smaller than 50% in the region depicted in Fig. 5. This precision, however, is higher than that of measured galaxy peculiar in a volume this size and so we cannot compare our model predictions with velocity data over the entire region of Fig. 5. A reliable comparison is only possible over a smaller volume, typically of radius $\sim 80 h^{-1}$ Mpc. For this reason we now describe in some detail our reconstructions within this distance.

4.1 The PSCz model density and velocity fields within $80 h^{-1}$ Mpc

Fig. 6 shows the PSCz model density and velocity fields smoothed with a $6h^{-1}$ Mpc Gaussian in a slice through the Supergalactic plane. With this smoothing, the Local Supercluster, centered on the Virgo cluster at $(\text{SGX}, \text{SGY}) = (-2.5, 11.5)$, does not appear as an isolated structure but is connected instead to the prominent Hydra–Centaurus supercluster at $(\text{SGX}, \text{SGY}) = (-35, 20)$. Together with the Pavo–Indus–Telescopium supercluster [$(\text{SGX}, \text{SGY}) = (-40, -15)$], the latter makes up the well known Great Attractor. The Coma cluster and its neighbour, A1367, appear as a peak at $(\text{SGX}, \text{SGY}) = (0, 75)$, slightly elongated in the SGX direction. The Perseus–Pisces supercluster, clearly visible at $(\text{SGX}, \text{SGY}) = (45, -20)$, is the second largest peak on the map, well separated from its northern extension [$(\text{SGX}, \text{SGY}) = (45, 20)$] which is sometimes called the Camelopardalis supercluster. Finally, the Cetus Wall may be seen as an elongated structure around $(\text{SGX}, \text{SGY}) = (15, -50)$. The Sculptor void [$(\text{SGX}, \text{SGY}) = (-20, -45)$] is the largest underdensity in the map, but is almost matched in size by a void in the background of the Camelopardalis supercluster. Three more underdense regions that exert an important influence on the local dynamics are the voids in the foreground of Coma [$(\text{SGX}, \text{SGY}) = (-10, 50)$], in the background of the Perseus–Pisces complex [$(\text{SGX}, \text{SGY}) = (50, -50)$], and behind the Great Attractor [$(\text{SGX}, \text{SGY}) = (-60, 10)$].

The competing dynamical roles of the various overdense and underdense structures seen in Fig. 6. determine the local velocity field in a complex manner that cannot be simply described as a bulk flow or by a multi-spherical infall model. The local velocity field implied by the PSCz density field is illustrated by the vectors plotted in Fig. 6. Its dominant features are the large infall patterns towards the Great Attractor, Perseus–Pisces, Cetus Wall and Coma. A striking property is the large-scale coherence of the velocity field, apparent as a long ridge between Cetus and Perseus–Pisces and as a large-scale flow along the Camelopardalis, Virgo, Great Attractor baseline and beyond (see §5). A prediction of the PSCz data is the lack of prominent back-infall onto the Great Attractor region. The flow around it appears to be determined by the compressional push of two voids (at $(\text{SGX}, \text{SGY}) = (-10, 50)$ and $(-60, 10)$) and the pull of the Shapely Concentration on much larger scales (see §5). All these features are also present when Method 2 is used for the reconstruction (§4.2), or when the 1.2Jy survey is used as the input catalogue (§4.3). As pointed out by Davis, Nusser & Willick (1996), this model velocity field does not match the Mark III peculiar velocity field (Willick *et al.* 1997a) which exhibits a large outflow away from the Centaurus supercluster and an inflow onto the Hydra complex. There is also no evidence for a motion of the Perseus Pisces supercluster towards us.

Fig. 7 extends our qualitative analysis to two planes of constant SGZ, $40h^{-1}$ Mpc above and below the Supergalactic plane. The slice at $\text{SGZ} = +40 h^{-1}$ Mpc shows a region which is largely underdense (Fig 7b), dominated by a void which is connected to the Local Void identified by Tully (1987). The prominent peak at $(\text{SGX}, \text{SGY}) = (40, -30)$ seems to be an extension of the Perseus–Pisces supercluster and the one at $(\text{SGX}, \text{SGY}) = (-50, 20)$ appears to be connected to the Pavo–Indus–Telescopium complex. Overall the density field traced by the PSCz survey looks remarkably similar to the one obtained from the IRAS 1.2Jy catalogue (see §4.3 and the analogous discussion by Strauss and Willick 1994). The velocity field (Fig 7a) is still characterized by a coherent, large-scale, flow towards the same direction [$(\text{SGX}, \text{SGY}) = (-50, 50)$] as the stream seen in the Supergalactic plane. At negative $\text{SGZ} = -40 h^{-1}$ Mpc the extensions of the Pavo–Indus–Telescopium $(-50, 15)$ and Perseus–Pisces $(20, -20)$ superclusters are visible. The dynamical effect of these two peaks is evident in the associated large infall patterns (Fig. 7c).

4.2 Comparison of the two reconstruction methods

A detailed quantitative error analysis of mock PSCz catalogues performed by Branchini *et al.* (1998) also shows that the predicted velocity field is not affected by any significant systematic bias. To check this result further we have compared the reconstructions produced by the two different methods discussed in §3.1. The two upper plots in Fig. 8 show the predicted velocity fields smoothed with a $6h^{-1}$ Mpc Gaussian in a slice through the Supergalactic plane. The two methods succeed in reproducing the main features that we have already highlighted: remarkable large-scale coherence in the velocity field, clear infall patterns onto Coma, Perseus–Pisces and the Great Attractor but no back-

infall onto the latter. The only noticeable difference is that Method 2 seems to blur slightly the sharp features (like the Cetus ridge) produced by Method 1 in the velocity field.

Quantitative evidence for the similarity of the two model fields is provided in the lower part of Fig 8, which shows a scatterplot of the SGY Cartesian components of the reconstructed velocity fields, smoothed with a $6h^{-1}$ Mpc Gaussian, measured within $80h^{-1}$ Mpc. For both model velocity fields we have used $\beta = 1$. In the plots we show only 1000 points taken at random from the 73490 available. The peculiar velocities in the two models should obey the linear equation,

$$M_2 = BM_1 + A, \quad (11)$$

where M_1 and M_2 denote any of the Cartesian components of the peculiar velocity predicted by Methods 1 and 2, respectively, and B is expected to be 1 if no systematic errors are present. The offset A allows for possible differences in the predicted bulk flows in the two models. We obtain the values of A and B by minimizing

$$\chi^2 = \sum_{i=1}^{N_t} \frac{(M_{2,i} - A - BM_{1,i})^2}{(\sigma_{M_1,i}^2 + B^2\sigma_{M_2,i}^2)}, \quad (12)$$

where $\sigma_{M_1,i}$ and $\sigma_{M_2,i}$ are the errors in the velocities at a generic gridpoint i in the two methods, and N_t is the total number of points used for the comparison. We assume that $\sigma_{M_1,i} = \sigma_{M_2,i} \equiv \sigma$, so that eqn.(12) becomes

$$\chi^2 = \frac{1}{\sigma^2} \sum_{i=1}^{N_t} \frac{(M_{2,i} - A - BM_{1,i})^2}{(1 + B^2)} = \frac{\chi_o^2}{\sigma^2}. \quad (13)$$

Only N_i of the N_t points used in the comparison are independent. It can be shown that the quantity $\chi_{eff}^2 = (N_i/N_t)\chi^2$ is approximately distributed as χ^2 with $N_{d.o.f} = N_i - 2$ degrees of freedom (e.g. Hudson *et al.* 1995). We can therefore approximately evaluate σ by setting $\chi_{eff}^2 = N_{d.o.f}$ so that

$$\sigma^2 = \frac{\chi_o^2 N_i}{N_t(N_i - 2)}. \quad (14)$$

We take N_i to be the number of independent volumes within the volume sampled. With our smoothing radius, $N_i \simeq 6300$. We then find a regression slope, $B = 0.98 \pm 0.06$. The zero point, $A = -47 \pm 5$, indicates a systematic difference in the SGY component of the bulk velocity in the two models. This offset is only evident when the two velocity fields are compared in the CMB frame and almost disappears in the Local Group (LG) frame. As explained in §3, the peculiar velocities are reconstructed in the LG frame. Transformation to this frame is performed by adding the reconstructed LG velocity at each galaxy position. This can lead to systematic differences if the LG velocities predicted by the two methods do not agree. Indeed, the zero point offset measured in the velocity–velocity scatterplot for the three Cartesian components, $(-123, -47, 132)\beta \text{ km s}^{-1}$, is similar to the difference between the predicted LG velocities in the two models, $(-150, -50, 98)\beta \text{ km s}^{-1}$. No other systematic errors are detected as the regression slopes are close to one also for the two remaining components (0.97 ± 0.06 for SGX and 1.06 ± 0.05 for SGZ.) For the SGX and SGZ components, the dispersions around the fit are only slightly larger than for SGY ($\sigma = 61, 54, 70)\beta \text{ km s}^{-1}$ respectively.) This represents the intrinsic error in the reconstruction and is nearly a factor of 2 smaller than the average total error derived from the error analysis on the mock PSCz catalogues (which also accounts for uncertainties in the filling in procedure, nonlinearity, finite volume effects, etc) by Branchini *et al.* (1998).

4.3 Comparison of the PSCz and 1.2Jy model velocity fields

Since they were drawn from the same parent catalogue, we expect the PSCz and 1.2Jy catalogues to give consistent model velocity fields, at least in the nearby volume where the sampling by 1.2Jy galaxies is not too sparse. In analogy with the PSCz fields displayed in Fig. 6, Fig. 9 shows the 1.2Jy density and velocity fields, smoothed with a $6h^{-1}$ Mpc Gaussian, in a slice through the Supergalactic plane. Most of the characteristic structures previously identified in Fig. 6 are also visible in Fig. 9 except that underdense regions in the 1.2Jy map appear somewhat more extended than in the PSCz map. The overall pattern in the PSCz velocity field is reproduced in the 1.2Jy map although the large-scale coherent flow along the Camelopardalis, Great Attractor baseline is less evident in the latter.

On the other hand, the infall pattern around the Great Attractor in the 1.2Jy survey spreads out over a larger region. These discrepancies might well be due to the larger shot noise in the 1.2Jy catalogue.

Our 1.2Jy model velocity field is consistent with that derived independently by Webster, Lahav and Fisher (1997) using the method developed by Fisher *et al.* (1995b). Comparison with their Fig. 7d (which assumes a CDM model with $\Gamma = 0.2$ as a prior in the Wiener filtering procedure) reveals only one noticeable difference between the two maps. This is in the region of the Great Attractor, where the model of Webster *et al.* predicts a weak back-infall. The discrepancy, however, is small and may simply reflect our use of a constant $6h^{-1}$ Mpc Gaussian smoothing, which is somewhat larger than the smoothing applied by Webster *et al.*

The lower part of Fig 10 displays the difference between the PSCz and the IRAS 1.2Jy overdensity fields, displayed in Figs. 6 and 9 respectively, $\Delta = \delta_{PSCz} - \delta_{1.2Jy}$. Positive (continuous lines) and negative (dashed lines) contours are shown, with the thick line delineating the $\Delta = 0$ contour. The main discrepancies between the two fields occur within the zone-of-avoidance, in the Great Attractor region and beyond. Outside the Galactic plane, the radially increasing shot noise is responsible for the large discrepancies seen in the outer regions. Apart from these local features, we notice that the mean value of Δ , $\langle \Delta \rangle$, is positive in the region shown in the figure. Indeed, this is true within the entire spherical volume of radius $70 h^{-1}$ Mpc in which we find $\langle \delta_{PSCz} \rangle = 7 \cdot 10^{-3}$ and $\langle \delta_{1.2Jy} \rangle = -6 \cdot 10^{-3} h^3 \text{Mpc}^{-3}$ (for both catalogues the average density has been measured within $100 h^{-1}$ Mpc). If the errors were due to sparse sampling alone, then this discrepancy would be significant at about the 2σ level. However, the errors in the estimates of the average density are larger than this. In particular, as pointed out by Davis, Strauss and Yahil (1991), the intimate coupling between the estimation of the selection function and the average density itself generates uncertainties in the reconstructed average density which are large enough to account for the discrepancy we have detected. The mismatch in the average densities on a scale of $70 h^{-1}$ Mpc generates the infall pattern visible in the upper panel of Fig 10, while smaller scale features originate from local mismatches between the two density fields.

Fig. 11 (lower panel) shows a more quantitative comparison between the PSCz and 1.2Jy overdensity fields, both smoothed with a $6h^{-1}$ Mpc Gaussian and tabulated onto 64^3 grids. The comparison is made in the CMB frame and assumes $\beta = 1$. Only those gridpoints within $80 h^{-1}$ Mpc of the LG position are considered. As in the previous section, we fit a straight line to the data and estimate the parameters by minimizing χ^2 . The slope of this line is 1.08 ± 0.8 , indicating that there are no systematic differences between the two density fields. The negative zero point offset, -0.5 ± 0.03 , reflects the discrepancy between the average densities of the two catalogues discussed in the preceding paragraph ($\Delta\delta = -0.05$). The scatter $\sigma_\delta = 0.20$ is similar to the average shot noise at the gridpoint positions both for PSCz ($\sigma_{SN} = 0.18$) and for the IRAS 1.2 Jy ($\sigma_{SN} = 0.24$) catalogues. Similar considerations apply to the velocity-velocity comparison in the upper panel in which, as in Fig 8, we only show the SGY Cartesian component of the velocity. The comparison, performed in the CMB frame, assumes $\beta = 1$. There is a non-negligible zero point offset of $(56 \pm 8)\beta \text{ km s}^{-1}$ which is comparable to the difference between the SGY components of the predicted LG velocities for two catalogues ($80\beta \text{ km s}^{-1}$). The dispersion around the fit, $\sigma_v = 104\beta \text{ km s}^{-1}$, is again similar to the average shot noise in the peculiar velocities, computed as in Yahil *et al.* (1991) ($88\beta \text{ km s}^{-1}$ for PSCz and $140\beta \text{ km s}^{-1}$ for IRAS 1.2Jy). Similar results are found from the scatterplots of the two remaining Cartesian components. Their slopes are consistent with unity (1.06 ± 0.6 and 0.91 ± 0.08 for SGX and SGZ respectively) and the zero point offsets are comparable to the discrepancies arising from the transformation from LG to CMB frames (153β and $118\beta \text{ km s}^{-1}$).

Finally, Tadros *et al.* (1998) have recently suggested that the PSCz catalogue should not be used down to 0.6 Jy and that a more conservative cut in flux, 0.745 Jy, should be adopted instead. To check whether possible incompleteness at the low flux limit could affect the modeling of the PSCz velocity field we have generated several different models for density and velocity fields using a suite of PSCz subcatalogues taken at different flux limits. With a 0.75 Jy cut the density and velocity fields are still remarkably similar to those with the cut at 0.6Jy. Increasing the flux limit makes the PSCz density and velocity fields more and more like the IRAS 1.2 Jy fields with which they almost coincide when the cut is taken at 1.2 Jy. Overall, our prediction for the PSCz velocity and density fields are robust and are not affected by incompleteness in the catalogue at low flux levels, at least within a region of $200 h^{-1}$ Mpc.

5 MODELLING VERY LARGE SCALE MOTIONS

The sampling density of the PSCz survey is high enough to allow investigation of the density field out to $\sim 120 h^{-1}$ Mpc even with a $6h^{-1}$ Mpc Gaussian smoothing. This is illustrated in Fig. 12 which displays the usual section of the density and velocity model along the Supergalactic plane. The shot noise in this map is the same as in the maps discussed in §4.1. The larger volume reveals the full extent of the coherent streaming involving galaxies from the Camelopardalis Supercluster all the way to the Shapley Concentration (that begins to become visible at $(SGX, SGY) = (-100, +60)$), passing through the Local Supercluster and the Great Attractor.

The dynamical sources of the coherent motion seen in Fig. 12 are the same ones that we identified earlier as being responsible for the flow pattern behind the Great Attractor. The gravitational pull is mostly due to the Shapley Concentration, but the coherence is aided by the combined push of the two large voids (at $(SGX, SGY) = (-80, 10)$ and $(SGX, SGY) = (-50, 70)$) that straddle the ridge and were only partially visible in Fig. 6. This map also reveals a large extension to other underdense regions, the Sculptor void and the two connected voids behind the Cetus–Perseus–Pisces–Camelopardalis complex.

In Fig. 13 we show slices along four planes parallel to the Supergalactic plane, at $SGZ = \pm 40$ and $SGZ = \pm 80$. Fig. 14 shows the corresponding velocity fields. The same structures that we had identified in Fig. 7 can now be traced over larger scales. The shot noise is still small and so we can fully appreciate the large scale coherence of features in both the density and velocity fields. For example, Figs. 13a and 13b show that the void that we had identified in the upper half of Fig. 7b actually extends over a much larger volume. Similarly, the stream towards $(SGX, SGY) = (-50, 50)$ that we had identified in the $SGZ = 0$ and $SGZ = +40 h^{-1}$ Mpc planes persists at $SGZ = +80 h^{-1}$ Mpc. No very large scale features are present in the plane at $SGZ = -40 h^{-1}$ Mpc (Fig. 13c and 14c) which, as we had previously noted, is dominated by a few isolated infall patterns onto the southern extensions of the Pavo–Indus–Telescopium and Perseus–Pisces superclusters. New large coherent structures, however, begin to appear again in the plane at $SGZ = -80 h^{-1}$ Mpc.

5.1 Comparison with the Abell/ACO model fields

Various surveys of IRAS and optical galaxies have been used to construct model velocity fields which proved to be remarkably consistent with one another (Yahil *et al.* 1991, Kaiser *et al.* 1991, Hudson 1994, Baker *et al.* 1998). We carry out a similar exercise here, using a completely different set of mass tracers, the Abell/ACO clusters. With these we can model the density and velocity fields out to very large scales, albeit with much larger sampling errors. BP96 have already employed the same Abell/ACO cluster subsample described in §2 to model the density and velocity fields out to $250 h^{-1}$ Mpc. The reconstruction technique they used is a simplified version of our Method 1 (cf. §3.1) in which the selection function (which is nearly constant on the scales of interest) is not iteratively updated, no special treatment is given to triple-valued regions and the procedure for filling in the zone-of-avoidance ($|b| \leq 20^\circ$) is the one used by Yahil *et al.* (1991). In order to compare the PSCz and cluster model fields we smooth both with a Gaussian filter of width $20 h^{-1}$ Mpc. Such a large smoothing is required because of the large intercluster separation.

Fig. 15 shows the smoothed density fields along the Supergalactic plane, within a distance of $150h^{-1}$ Mpc, derived from the PSCz (upper panel) and cluster (lower panel) catalogues. Overdensity contours are plotted in steps of $\Delta\delta = 0.2$ for the galaxy field, and of $\Delta\delta = 0.88$ for the cluster field. This is equivalent to rescaling the cluster field by a factor $b_c = 4.4$ which, as we shall see in §5.2 below, is our estimate for the relative linear bias parameter between IRAS galaxies and galaxy clusters. As before, the heavy line traces the $\delta = 0$ contour. The dashed lines show the approximate location of the zone-of-avoidance in the PSCz ($|b| \leq 8^\circ$) and cluster ($|b| \leq 20^\circ$) samples.

Despite the $b_c = 4.4$ rescaling, the density peaks appear more prominent in the cluster sample than in the PSCz map. This may reflect more severe undersampling of the cores of rich clusters by IRAS galaxies than was indicated by Baker *et al.* (1998), or it may be due to shot noise in the cluster sample which, in spite of the heavy smoothing, is still substantial. It should be noted, however, that the Great Attractor region $(SGX, SGY) = (-50, 0)$ and the Perseus–Pisces supercluster $(SGX, SGY) = (50, -20)$, where the effect is strongest, both lie within the zone-of-avoidance of

the cluster sample. It is therefore possible that the height of these peaks has been artificially amplified by the coupling between shot noise and the filling-in procedure. For this reason we shall exclude the region at $|b| \leq 20^\circ$ from the quantitative analysis in §5.2 below. Above $|b| = 20^\circ$ the Shapley Concentration (SGX, SGY) = $(-120, 70)$ is the only peak with a larger amplitude in the cluster map than in the PSCz map. Amplitudes aside, the positions of the peaks in the two density maps are very similar. The low density regions are also approximately coincident, although they are less extended in the cluster map in which voids also appear somewhat shallower. The latter effect simply reflects the fact that the assumption of local biasing, $\delta_c = b_c \delta_g$, breaks down at low δ_g because of the constraint $\delta_c \geq -1$.

Similar considerations apply outside the Supergalactic plane. Fig 16 extends the comparison between clusters (left-hand side) and PSCz galaxies (right-hand side) to four slices parallel to the Supergalactic plane, at $\text{SGZ} = \pm 45 h^{-1} \text{Mpc}$ and $\text{SGZ} = \pm 100 h^{-1} \text{Mpc}$. Although some discrepancies in the position of peaks and voids exist, the large-scale features are remarkably similar across all the slices. In particular, the large overdense region at positive SGZ is evident in both the clusters and PSCz density fields. Unlike in the Supergalactic plane, there appears to be no appreciable systematic difference between the amplitudes of density peaks of clusters and IRAS galaxies.

Fig. 17 shows the velocity fields inferred from the two samples, again with a $20h^{-1} \text{Mpc}$ Gaussian smoothing, in a slice along the Supergalactic plane. The amplitude of the velocity vectors is on an arbitrary scale but, for the clusters, the velocities have been rescaled by the factor $b_c = 4.4$. The two large overdensities lying within the zone-of-avoidance in the lower panel of Fig. 15 largely determine the infall patterns at those locations $[(\text{SGX}, \text{SGY}) = (-50, 0)]$ and $[(\text{SGX}, \text{SGY}) = (50, -20)]$. Beyond $|b| = 20^\circ$, however, the galaxy and cluster velocity fields are very similar. Both exhibit a large coherent flow along the Camelopardalis, Great Attractor, Shapley Concentration baseline. The infall onto the Shapley region is more prominent in the cluster map but, in general, the velocity field patterns are very similar at positive SGY, with an outflow at positive SGX, and a convergent flow towards the Shapley Concentration at negative SGX. Below the zone-of-avoidance, at negative SGY, both maps show outflow from the Sculptor void, but this is less prominent in the clusters map.

Note that a similar good agreement would have been obtained by considering the density-velocity maps by Scaramella (1995) which also use the Abell/ACO cluster distribution.

5.2 The relative linear bias between galaxy clusters and IRAS galaxies.

If biasing is a local process then, in the regime where mass fluctuations are small, we expect the amplitude of the bias to be independent of scale (see e.g. Cole *et al.* 1998). This expectation is consistent with the results of POTENT analyses performed by Dekel *et al.* (1993) and Sigad *et al.* (1998) and we expect it also to be valid in the present analysis in which the PSCz and cluster density and velocity fields have been smoothed with a $20h^{-1} \text{Mpc}$ Gaussian filter. Thus, on the scales of interest, we expect the two model density and velocity fields to be linearly related:

$$C = Pb_c + A_c, \quad (15)$$

where C and P stand for cluster and PSCz and represent either δ or any one of the Cartesian components of the velocity field. The constant b_c is the bias parameter of clusters relative to IRAS galaxies and A_c allows for a relative offset in the mean density or bulk velocities of the two fields. For quantitative analyses it is most convenient to use the SGY Cartesian component of the velocity field since this is the least affected by uncertainties in filling in the zone-of-avoidance. To estimate b_c we adopt the strategy of Hudson *et al.* (1995) and Branchini *et al.* (1997), already used in §4.2, of regressing the two model fields by minimising the quantity

$$\chi^2 = \sum_{i=1}^{N_t} \frac{(C_i - A_c - b_c P_i)^2}{(\sigma_{C,i}^2 + b_c^2 \sigma_{P,i}^2)}, \quad (16)$$

where the subscript i refers to any of the N_t gridpoints within the comparison volume. The quantities $\sigma_{C,i}$ and $\sigma_{P,i}$ represent the errors in the cluster and PSCz fields, respectively.

The errors in the cluster field, $\sigma_{C,i}$, have been estimated by Branchini *et al.* (1997). They are the sum in quadrature of the intrinsic errors in the reconstruction procedure, as estimated by BP96 using Montecarlo techniques, and the

shot noise uncertainties which are dominant for the very sparse cluster fields. The latter were evaluated using the mock catalogue generated by Kolatt *et al.* (1996) which is designed to reproduce the distribution of structures in our local universe. A typical error in the cluster overdensity field is $\langle\sigma_{C,\delta}\rangle = 0.36$, and in the SGY-component of the velocity field it is $\langle\sigma_{C,v_y}\rangle = 250\beta \text{ km s}^{-1}$.

The errors in the PSCz fields have been estimated using the mock catalogues described in §3.2. The basic procedure consists of comparing the density and velocity fields obtained by applying Method 1 to the mock galaxy catalogues with the true fields in the parent N-body simulation. Fig. 18 (which is analogous to Fig. 4) compares the true and reconstructed density and velocity fields of a mock PSCz catalogue (different from the one shown in Fig. 4) in a slice along the Supergalactic plane (upper panels). The maps of the density and velocity errors are shown in the lower panels. Both fields are smoothed with a Gaussian filter of radius $20 h^{-1} \text{ Mpc}$. As in Fig. 4, the errors in the density and velocity reconstruction occur preferentially within the zone-of-avoidance. However, the correlation with the signal, which was present in the outer regions of Fig. 4, has been almost erased by the large smoothing. We have characterized the reconstruction errors by noticing that the residuals correlate with distance, galactic latitude and, for the velocity field, with the signal itself. From the analysis of the mock catalogues, we have derived two approximate expressions for the errors (valid for $|b| > 20^\circ$):

$$\langle\sigma_{P,\delta}\rangle = 0.11 - 6.7 \cdot 10^{-4} \cdot |b| + 3.3 \cdot 10^{-4} \cdot r \quad (17)$$

and

$$\langle\sigma_{P,v_y}\rangle = 70 + 2.7 \cdot 10^{-1} \cdot r + 0.15 \cdot |v_y|, \quad (18)$$

where r is the distance measured in $h^{-1} \text{ Mpc}$, b is the galactic latitude in degrees (not the linear biasing factor), and $|v_y|$ is the amplitude of the SGY Cartesian component in km s^{-1} . The actual assumed error at a gridpoint has been generated from a Gaussian distribution centred on $\langle\sigma_P\rangle$ with dispersions of 0.04 for the overdensity and 40 km s^{-1} for the v_y field, respectively.

The regression of the PSCz and cluster fields uses all the gridpoints within $120 h^{-1} \text{ Mpc}$ and outside the cluster zone-of-avoidance (i.e. at $|b| > 20^\circ$). As a result of the large smoothing applied, not all the gridpoints in the comparison volume are independent. The number of independent points, N_i , can be computed as in Dekel *et al.* (1993),

$$N_i^{-1} = N_t^{-2} \sum_{j=1}^{N_t} \sum_{i=1}^{N_t} \exp(-r_{ij}^2/2R_s^2), \quad (19)$$

where r_{ij} is the separation between gridpoints i and j and R_s is the smoothing radius of the Gaussian filter. This expression has been derived for a smooth density field and its application to a velocity field requires some caveats. For a given comparison volume, the large coherence of the velocity field causes the number of independent points to be smaller than N_i . On the other hand, our peculiar velocities are predicted using a sample covering a larger volume than that used in the comparison and this increases the number of independent points. Because of these competing effects, we simply approximate the number of independent points by N_i , even in the $v-v$ comparison.

As in §4.2 we define the $\chi_{eff}^2 \equiv (N_i/N_t)\chi^2$ statistic which corresponds, in practice, to multiplying the errors σ_P and σ_C by $\sqrt{N_t/N_i}$ in equation (16). We use this statistic to estimate the errors in b_c and A_c .

Fig. 19 (upper panel) shows a δ - δ scatterplot of the model cluster and PSCz overdensity fields measured at ~ 1000 randomly selected gridpoints. All 6426 original points are used in the regression analysis. The solid line shows the best fit obtained by minimizing χ_{eff}^2 and the parameters of the fit are listed in Table 3. The resulting bias parameter is $b_c^\delta = 4.4 \pm 0.6$. This is consistent with results from an independent likelihood analysis in which the phenomenological power spectra of IRAS galaxies and Abell clusters were compared (e.g. Peacock and Dodds 1994). The parameter $S^\delta = \chi_{eff}^2/N_{dof} = 1.14$, which may be taken as an indication that the errors have not been grossly over- or underestimated. The systematic difference in the amplitude of the density peaks in the cluster and IRAS δ fields, noticed in Fig 15, manifests itself as a deviation from the best fitting line at large δ_{PSCz} . Restricting the regression to values of $\delta_{PSCz} \leq 0.35$ returns $b_c^\delta = 4.5 \pm 0.6$, almost identical to the previous value, and $S^\delta = \chi_{eff}^2/N_{dof} = 1.15$. This suggests that the exact weighting of PSCz galaxies in high density regions has only a minor effect on the regression

analysis, mainly because the overdensity mismatch in large density peaks is restricted to a very few gridpoints. As a further check, we have repeated the δ - δ regression using a PSCz velocity model derived without applying our standard procedures for collapsing clusters and handling triple valued regions (which should exacerbate any discrepancies associated with high peaks.) The results, listed in the second row of Table 3, show that the effect on b_c is indeed very small, leading to $b_c^\delta = 4.5 \pm 0.6$.

The lower panel of Fig. 19 shows the scatterplot of the SGY Cartesian components of the two velocity fields in which, as in the upper panel, to avoid overcrowding, we only show ~ 1000 randomly selected gridpoints. As shown in Table 3 the slope of the best fitting line is $b_c^{v_y} = 4.7 \pm 0.6$ with no significant zero point offset, indicating that the SGY components of the cluster and PSCz bulk flows are consistent with one another over the scales of interest. However, as indicated in Table 3, the resulting χ_{eff}^2 is large, $S^{v_y} = 1.55$. This could be due to an underestimate of the errors since the error analysis by Branchini *et al.* (1997) is based on clusters from the Kolatt *et al.* (1996) mock catalogues and these do not accurately match the Abell/ACO cluster distribution and velocities. We can obtain $S^{v_y} \simeq 1.0$ if we allow for a reasonable error underestimate in the cluster field of $\sim 30\%$, in which case we obtain $b_c^{v_y} = 4.0 \pm 0.6$. Note that consistent values of b_c^δ and $b_c^{v_y}$ are obtained within $1\text{-}\sigma$ whether or not the cluster errors have been underestimated at this level.

It is worth emphasizing that the agreement of the δ - δ and v_y - v_y comparisons is not trivial. The δ - δ comparison is local; it is hardly affected by problems related to filling in masked regions but is potentially prone to the cluster core weighting problem. The v_y - v_y comparison, on the other hand, involves the distribution of objects within the entire sample and thus is much more strongly affected by the unknown mass distribution within the zone-of-avoidance and beyond the sample's edge. We might therefore expect the two comparisons to be subject to different biases. The agreement in the estimates of b_c from the two analyses suggests that systematic biases have been properly taken into account and that the linear biasing assumption is a good approximation, at least on scales larger than our $20 h^{-1}$ Mpcsmoothing.

6 THE BULK VELOCITY VECTOR

In this section we consider the peculiar velocity, $\mathbf{v}_b(R)$, of spheres of radius R centred on the Local Group. This is a low order statistic that, in principle, can be estimated observationally. The expectation value of the bulk velocity, $|\mathbf{v}_b|$, averaged over scale R is:

$$\langle |\mathbf{v}_b(R)|^2 \rangle = \frac{\beta^2 H_0^2}{2\pi^2} \int P(k) W(kR)^2 dk, \quad (20)$$

where $P(k)$ is the power spectrum of density fluctuations, $W(kR) = 3 \frac{\sin(kR) - kR \cos(kR)}{(kR)^3}$ is the Fourier transform of the spherical top hat window function in real space, chosen to facilitate comparison between the theoretical definition (eqn. 20) and its observational analogue (eqn. 21). It is worth stressing that eqn.(20) assumes equal volume weighting while the use of different weighting schemes may lead to quite different results (Kaiser 1988, Strauss et al. 1995, Giovanelli et al. 1998). If the initial fluctuation field obeys Gaussian statistics, then evolution through gravitational instability preserves a Gaussian distribution for the amplitude of each Cartesian component of $\mathbf{v}_b(R)$, so that $|\mathbf{v}_b(R)|$ has a Maxwellian distribution. This property makes it difficult to constrain $P(k)$ from the measured $\mathbf{v}_b(R)$. Nevertheless, comparison of the measured $\mathbf{v}_b(R)$ with the velocities predicted from the PSCz gravity field allows, in principle, an estimate of the β parameter. In practice, however, the bulk velocity is extremely sensitive to systematic errors both in the observational data and in the models. We attempt to take this carefully into account in the following analysis.

6.1 The model bulk flow

The basis for our treatment of random and systematic errors in the model bulk velocity vector are, again, the mock PSCz catalogues described in §3.2. Finite volume effects are not a concern here since the volume of the simulation

box is comparable to that of the PSCz sample. However, neglecting modes on scales larger than the size of the sample can bias the comparison between the model bulk flow and the measured one. In what follows we will treat these two effects separately. We first account for the intrinsic errors in the bulk flow model and we then address the problem of minimizing the effect of missing large-scale power.

From each mock catalogue we generate a model velocity field using Methods 1 and 2 of §3.2. The field is then smoothed onto a 64^3 cubic grid of side $192 h^{-1}$ Mpc using a $12h^{-1}$ Mpc Gaussian filter. The smoothing filter used here is different from the one used before because our aim is to perform a homogeneous comparison with the Mark III and SFI bulk flows. We measure the cumulative bulk velocity vector in the CMB frame by averaging over the peculiar velocities measured at gridpoints:

$$\mathbf{v}_b(R) = \frac{\sum_{(i,j,k) < R} \mathbf{v}_{i,j,k}}{\sum_{(i,j,k) < R}}, \quad (21)$$

where $\mathbf{v}_{i,j,k}$ is the predicted velocity vector in the CMB frame at gridpoint (i, j, k) . The sum $\sum_{(i,j,k) < R}$ extends over all the gridpoints contained within a sphere of radius R . The same exercise is repeated using the original N-body velocity field. This gives an unbiased estimate of the true bulk velocity and the comparison between true and reconstructed velocities is an estimate of the error in the PSCz model bulk flow.

In the upper panel of Fig. 20 we show the average difference between reconstructed and true cumulative bulk velocity vectors. Each Cartesian component is displayed with a different symbol. The errorbars, representing the dispersion around the mean, are shown only for the SGY component. The dispersions for the remaining two components are larger by nearly a factor of two. From the plot we see that the errors in the SGY and SGZ components of the reconstructed bulk flow are mainly random errors, but the SGX component is affected by a systematic positive bias. The amplitude of this systematic error decreases with distance (from $\sim 61 \text{ km s}^{-1}$ at $10 h^{-1}$ Mpc to $\sim 16 \text{ km s}^{-1}$ at $100 h^{-1}$ Mpc). Very similar results are obtained if the reconstruction is carried out using Method 2. These systematic errors arise mainly from the filling-in procedure for the zone-of-avoidance which, as we discussed in §3.2, affects both the velocity fields and, via uncertainties in modeling the LG velocity, the transformation from LG to CMB frame. To corroborate this hypothesis we have performed 10 reconstructions using unmasked mock catalogues. With full sky coverage, the systematic bias in the SGX component disappears and the dispersions in the SGX and SGZ components decrease by a factor of two. The systematic error in the SGX component is ultimately induced by the requirement of having only LG-like observers in the PSCz mock catalogues. In particular, visual inspection reveals that the galaxy dipole constraint in §3.2 almost invariably implies the existence of a Great Attractor-like density peak at a distance of $30\text{--}60 h^{-1}$ Mpc, lying at negative SGX and partially overlapping the zone-of-avoidance. The filling-in procedure seems to underestimate the amplitude of this partially hidden density peak and this in turn causes a systematic offset in the SGX component of the reconstructed peculiar velocities, with minor effects on the two other components, as shown in Fig. 20. A similar bias is to be expected in the true model PSCz bulk flow because the Great Attractor really exists in our universe. To obtain bias-free estimates of the PSCz bulk flows, we must correct for such systematic errors. Clearly, the best way of circumventing the problem is by restricting attention to the SGY component of the bulk velocity. However, sometimes one is interested in the amplitude of the bulk velocity and, in this case, a direct numerical correction of the systematic error is appropriate.

Since the amplitude of the estimated errors depends on β , the errors displayed in the upper panel of Fig. 20 (or the analogous quantity for the velocity amplitude) cannot be directly used to make quantitative corrections to the PSCz model bulk flow. However, we can take advantage of the fact that, to first approximation, the model velocities scale linearly with β . Thus, the ratio between reconstructed and true bulk velocities should be independent of β . This ratio, averaged over our mock catalogues, is shown by filled circles in the lower panel of Fig. 20, as a function of distance, with errorbars again representing the dispersion around the mean. Since it is independent of β , this ratio may be used as a multiplicative factor to correct the predicted PSCz bulk flow amplitudes for systematic errors. As expected, the corrections become very small when considering the SGY component (open circles). We have performed a similar analysis to estimate errors in the PSCz bulk velocity obtained using Method 2 and in the 1.2Jy bulk flow model, obtained using Method 1.

We are now ready to derive model bulk flows and their uncertainties from the PSCz and 1.2Jy surveys. The upper left panel in Fig 21 shows the amplitude of the cumulative bulk velocity vector, predicted using various samples and methods. In all cases the bulk flow was computed by integrating the density field out to the same distance of $200 h^{-1} \text{ Mpc}$, hence enforcing the same volume bias in all cases. The velocities are normalized to $\beta = 1$. Open and filled circles show PSCz results using Methods 1 and 2 respectively, and filled squares show results from the 1.2Jy survey, all corrected for systematic errors as discussed in the preceding paragraph. For clarity only the $1\text{-}\sigma$ error bars from Method 1 are plotted. The filled triangles show the bulk velocity computed from the Abell/ACO model velocity field, rescaled by $b_c = 4.4$ (see §5.2). There is remarkably good agreement between the cumulative bulk flows computed from the different sets of mass tracers, with typical deviations of less than $\sim 20\%$ from the mean in the amplitude from the different surveys and analysis methods. The directions of the cumulative bulk flow vectors, measured within $60 h^{-1} \text{ Mpc}$, are plotted in the upper right-hand panel of Fig. 21. The PSCz model bulk flow points, within 1σ , to the direction of both the 1.2Jy and Abell/ACO model bulk flows. The direction of the CMB dipole, indicated by the asterisk, is plotted for reference at the centre of the figure. In the lower panel of Fig. 21 we show the misalignment angle of the various bulk flows with respect to the PSCz –Method 1 model. In all cases the misalignment is small and almost independent of radius. The only exception is the increasing misalignment angle at large radii between the PSCz bulk velocities determined using Method 1 and Method 2. Note the close alignment between the PSCz and clusters bulk flows at all radii.

So far we have modelled bulk velocities in the nearby universe by considering only the gravitational effect of the mass distribution within $200h^{-1} \text{ Mpc}$. Bulk flows, however, are sensitive to the mass distribution on scales larger than those probed by our samples. Neglecting large scale modes leads to a volume bias which can affect the comparison with observations. Various methods have been proposed to restore the missing large scale modes (e.g. Strauss *et al.* 1995, Tormen and Bertschinger 1996, Cole 1997). Here we propose a simple statistical treatment based on linear theory, using eqn. (20) to obtain a correction factor for the missing contribution to the amplitude of the bulk velocity from scales beyond the sample boundary. The correction factor is the ratio

$$F(P(k), k_{min}) = \frac{\int_0^\infty P(k)W(kR)^2 dk}{\int_{k_{min}}^\infty P(k)W(kR)^2 dk}. \quad (22)$$

The numerator in this equation is the mean true bulk flow, while the denominator is the mean bulk flow generated only by density fluctuations on scales smaller than $R_{max} = \frac{2\pi}{k_{min}}$. In our case, $R_{max} \sim 200h^{-1} \text{ Mpc}$. Note that the ratio depends only on the spectral shape and on k_{min} ; the dependence on β cancels out. Tests using large N-body simulations (e.g. Jenkins *et al.* 1998) have shown that this approach is indeed effective. Since the amplitude of the bulk flow follows a Maxwellian distribution, and its components are Gaussian random variables, we can numerically estimate the uncertainty in this correction. Assuming that these uncertainties and the intrinsic random errors computed above are uncorrelated, we obtain the total random uncertainties on the model bulk flow by adding them in quadrature. In computing F we assume a CDM model with spectral shape $\Gamma = 0.25$, as suggested by a wide variety of data on the large-scale galaxy distribution (e.g. Baugh 1996).

We have applied the correction of eqn. (22) to the bulk velocity reconstructed from the PSCz survey using Method 1. The resulting cumulative bulk velocity (for $\beta = 1$) is shown in Fig. 21 as a dot-dashed line labelled M1L. We regard this as our best estimate of the β -dependent bulk flow.

6.2 Model vs. observed bulk flow

In this Section, we compare our best estimate of the predicted bulk flow velocity from the PSCz survey with recent observational estimates. This comparison serves two purposes. Firstly, consistency between predicted and observed velocities lends support to the hypothesis that structure grew by gravitational instability and gives confidence in the integrity of the observational data. Secondly, the comparison allows an estimate of the parameter $\beta = \Omega_0^{0.6}/b$.

The determination of bulk flows from peculiar velocity surveys is prone to systematic errors. For example, zero-point errors in the calibration of the distance indicators coupled with limited sky coverage may mimic a bulk

flow. Similarly, the coupling of large intrinsic errors in distance measurements with inhomogeneities in the density distribution (the inhomogeneous Malmquist bias) also results in a spurious outflow. Thus, to perform an unbiased comparison with theoretical predictions requires full-sky, homogeneous surveys of peculiar velocities and an accurate model of the survey's window function.

In Fig. 22 we plot observational determinations of bulk flows derived from four (almost) independent datasets. The lower panel shows the full cumulative bulk flow as a function of distance while the upper panel shows its SGY component only. The filled triangles (taken from Dekel *et al.* 1998) represent the cumulative bulk flows in the Mark III catalogue. The sparse and noisy Mark III velocities have been smoothed assuming that the velocity field is irrotational. This guarantees that a unique three-dimensional velocity field is derivable from the observed radial velocities, as in the POTENT method (Dekel, Bertschinger & Faber 1990). The resulting three-dimensional peculiar velocity field, smoothed with a $12h^{-1}$ Mpc Gaussian, and defined on a regular grid is directly comparable to our model prediction. The filled square shows the preliminary result by Eldar *et al.* (1998) who use a POTENT smoothing technique to derive the bulk velocity from the SFI catalogue (Giovanelli *et al.* 1997a, 1997b). The open triangle in the lower panel is the bulk velocity inferred from 44 supernovae Type Ia by Riess, Press & Kirshner (1995), as reported by Dekel (1997) (the effective radius of this last measurement is much smaller than the depth of the sample because the data were weighted by the inverse of the errors). Finally, the open square at large distance shows the bulk velocity derived by Lauer & Postman (1994; LP94) from a sample of brightest cluster galaxies. The directions of the observed bulk velocity vectors are given in the right-hand panel. For the Mark III, SFI and Sn 1a determinations, they have been estimated from data within $50 h^{-1}$ Mpc. The direction of the LP94 bulk flow is taken from Strauss (1997) and refers to a depth of $\sim 90 h^{-1}$ Mpc.

Except for the LP94 result, there is excellent agreement between the various determinations of the bulk flow in Fig. 22. These may be compared with the bulk flows predicted by the PSCz survey, indicated by the thick dot-dashed lines which enclose the $1-\sigma$ allowed range. These are normalized to $\beta = 0.75$ and corrected for volume bias. The filled circle in the right-hand plot marks the direction of the predicted bulk velocity vector within $50 h^{-1}$ Mpc.

Requiring that the predicted bulk flow should match the measured one gives an estimate of β . In performing this comparison we shall ignore the discrepant LP94 result which Strauss *et al.* (1995) and Watkins and Feldman (1995), amongst others, have argued is inconsistent with currently acceptable cosmological models. The LP94 data point is also inconsistent with our predicted bulk flow derived only from the gravitational instability and linear biasing hypotheses. Indeed, as shown in Fig. 22, matching the amplitude of the LP94 bulk flow would require a value of $\beta \simeq 1.9$, which is incompatible with all other current measurements (e.g. Giovanelli *et al.* 1998a, 1998b, Dekel *et al.* 1998 and Eldar *et al.* 1998) and implies a very large misalignment angle of 70° between the LP94 vector and the direction of our model flow velocity. In what follows we limit our comparison of model and observed bulk flows by imposing a series of restrictions designed to minimize possible systematic errors. These restrictions are:

- We consider only the cumulative bulk flow from Mark III as estimated by Dekel *et al.* (1998). Like the PSCz model velocity field, the Mark III velocities have been smoothed onto a regular grid and filtered on a similar scale. This ensures that the comparison is as homogeneous as possible.
- We consider Mark III peculiar velocities calibrated according to the recent VELMOD analysis by Willick and Strauss (1998).
- We exclude scales smaller than $30h^{-1}$ Mpc since small differences in the smoothing procedures applied to model and observed velocities in the nearby region can bias the comparison.
- We do not include the result of Eldar *et al.* (1998) which, although consistent with those of Dekel *et al.* (1998), is still preliminary.

We perform the comparison between model and observed bulk flows using a likelihood technique similar to that used by Strauss *et al.* (1992a) and Schmoldt *et al.* (1998). The aim is to estimate the likelihood of a particular value of β given the bulk flow observed in the Mark III catalogue and the one derived from the PSCz survey using Method 1. Under the assumption that the bulk velocities are Gaussian random fields it is easy to show that the joint probability distribution for the observed and model bulk flows is a multivariate Gaussian that depends only on its covariance

matrix. The latter is completely specified by the value of β and by the power spectrum of density fluctuations, $P(k)$. In this work we restrict attention to the family of CDM models for which $P(k)$, parametrised as in Davis *et al.* (1985), is completely specified by its shape parameter, $\Gamma = \Omega_0 h$, and normalization, σ_8 . Although the latter can be regarded as an independent parameter, adopting the normalization inferred by Eke, Cole, and Frenk (1996) from the observed abundance of galaxy clusters, allows one to relate σ_8 to Ω_0 . In the following we consider only two cases, $\sigma_8 = 0.52$ and 0.87 , which correspond to the cases of a critical, $\Omega_0 = 1.0$, and an open, $\Omega_0 = 0.3$, universe. (For a flat Universe with $\Omega_0 = 0.3$, the required value of σ_8 is similar).

Given a cosmological model specified by σ_8 , β , and Γ , we compute the joint probability of obtaining the cumulative bulk flow measured by Dekel *et al.* (1998) at 30, 40, 50 and 60 h^{-1} Mpc ($\mathbf{v}_M(i), i = 1, 4$), and the PSCz-M1 cumulative bulk flow displayed in Fig. 22, at all radii from 10 to 80 h^{-1} Mpc ($\mathbf{v}_P(j), j = 1, 8$). We ignore the correction for volume bias. The resulting probability density is:

$$f(\mathbf{v}_M(i), i = 1, 4, \mathbf{v}_P(j), j = 1, 8) = (2\pi)^{-3(4+8)/2} (\det M)^{-3/2} \exp\left(-\frac{1}{2} \mathbf{v}_l \cdot \mathbf{v}_m (M^{-1})_{lm}\right) d\mathbf{v}_M d\mathbf{v}_P, \quad (23)$$

where the covariance matrix M_{lm} is:

$$M_{lm} = \frac{1}{3} \langle \mathbf{v}_l \cdot \mathbf{v}_m \rangle = \frac{H_0^2 \beta^2}{6\pi^2} \int dk P(k) \tilde{W}_l(k) \tilde{W}_m(k). \quad (24)$$

The window functions are:

$$\tilde{W}_M(k) = 3 \frac{\sin(kr_i) - kr_i \cos(kr_i)}{(kr_i)^3} \quad (25)$$

for the Mark III cumulative bulk flow measured within r_i and

$$\tilde{W}_P(k) = 3 \frac{\sin(kr_j) - kr_j \cos(kr_j)}{(kr_j)^3} - 3 \frac{\sin(kR_s) - kR_s \cos(kR_s)}{(kR_s)^3} \quad (26)$$

for the PSCz cumulative bulk flow measured within r_j . In eqn. (26), $R_s = 200 h^{-1}$ Mpc represents the outer radius of the PSCz sample, i.e. the maximum distance out to which the PSCz density field is integrated to predict peculiar velocities. The second term in the right-hand side of eqn. (26) accounts for the volume bias affecting the M1-PSCz bulk flow. This correction is robust in the sense that the alternative strategy of limiting the integration in eqn. (24) to $k \geq k_{min} = 2\pi/R_s$ gives very similar results. Finally, we take into account random errors in the measured and modeled bulk flows by adding them in quadrature to the diagonal terms of the covariance matrix.

From the joint probability density distribution (eq. 23) we construct the relative likelihood, \mathcal{L} , of different world models (β, Γ, σ_8):

$$\mathcal{L} = -2 \ln(f). \quad (27)$$

The two plots in Fig. 23 show likelihood contours of $\mathcal{L}(\mathbf{v}_M(i), i = 1, 4; \mathbf{v}_P(j), j = 1, 8)$ in the $(\beta, l_{eq} = 1/\Gamma)$ plane, plotted at confidence levels of 68, 90 and 99 %. The shape of these contours is very similar for the two normalizations although the range of allowed values of β is somewhat larger for the high normalization. In both cases the likelihood peaks at $\beta = 0.6 - 0.7$; low values of β are excluded at high confidence level primarily by the requirement to match the amplitude of the observed bulk flow. No stringent constraint can be imposed on the shape parameter Γ apart from an upper limit that follows from the fact that the power cannot be confined to very small scales. The cluster normalization also defines a $(\beta, \Gamma) \rightarrow (b, h)$ transformation. Therefore, we can explore the effect of introducing an observational constraint on the Hubble parameter, ($0.4 < h < 0.8$), which defines a vertical region in the (β, Γ) plane. Introducing this extra constraint has a major effect in the case of low normalization since it forces the power to originate from unacceptably small scales. By contrast, in the case of high normalization, the extra constraint on h is perfectly consistent with the likelihood contours.

Following Schmoldt *et al.* (1998) we can set a more stringent constraint on β by considering not only the bulk flow but the entire set of observational information available on peculiar velocities in the local universe. In particular, we use the CMB dipole (\mathbf{v}_{LG}), the amplitude of the local velocity shear ($|\mathbf{v}_s|$), and the dipole in the gravitational acceleration induced by the distribution of PSCz galaxies in N independent radial shells ($\mathbf{v}_d(k), k = 1, N$) in order to compute the constrained probability function $f(\mathbf{v}_M(i), i = 1, 4; \mathbf{v}_P(j), j = 1, 8; \mathbf{v}_d(k), k = 1, N; \mathbf{v}_{LG} | \mathbf{v}_s)$. The

modeling of this probability distribution, its covariance matrix and the treatment of the errors may be found in Schmoldt *et al.* (1998) and Strauss *et al.* (1992a) to which we refer the reader for a more detailed discussion. In this analysis we use the PSCz differential dipole, \mathbf{v}_d , measured by Schmoldt *et al.* (1998) in $N = 15$ non-overlapping top-hat windows of width $10 h^{-1}$ Mpc and the same values of $\mathbf{v}_{LG} = 625 \pm 25$ and $|\mathbf{v}_s| < 200 \text{ km s}^{-1}$ used in §3.2.

The effect of adding these new observational constraints is shown in Fig. 24. The overall shape of the likelihood contours does not change appreciably. However, the valley along the Γ direction is now deeper and so the value of β is better constrained. This is clearly seen in Fig. 25 where we plot the distribution of the normalized likelihood of β obtained by marginalising the joint likelihood distribution over Γ . The continuous lines give the marginal distributions after integrating over all values of Γ , while the dot-dashed lines give the result of limiting Γ to the values allowed by the extra constraints on h . For $\sigma_8 = 0.87$, we find $\beta = 0.6_{-0.15}^{+0.22} (1-\sigma)$, irrespective of the constraint on h . Thus, in a low density universe, a power spectrum normalized according to the cluster abundance is consistent with the velocity data. By contrast, for the low normalisation, $\sigma_8 = 0.52$, the constraints on β change appreciably with the addition of the new constraints, leading to a larger value of $\beta = 0.9_{-0.20}^{+0.35} (1-\sigma)$. As may be seen in Fig. 24, however, in this latter case the relative probability within the strip allowed by the constraint on h is smaller than in the case of high normalization, thus rendering a high Ω_0 universe less likely according to the velocity data. Finally, it is interesting to note that the assumption of linear bias coupled with the cluster normalization of the power spectrum implies that $\beta \simeq 0.5/\sigma_8^{PSCz}$, irrespective of the value of Ω_0 . From the variance of the PSCz galaxy counts at $8 h^{-1}$ Mpc, $\sigma_8^{PSCz} \simeq 0.7$, and so we obtain $\beta \simeq 0.7$, consistent with the estimates above at the $1-\sigma$ level.

7 DISCUSSION AND CONCLUSIONS

The recently completed PSCz redshift survey of IRAS galaxies represents an almost ideal dataset for studying the mass distribution and the gravity field in the local universe. In this paper we have used the PSCz survey to develop a nonparametric model of the local cosmic velocity field which supersedes results derived from the shallower 1.2 Jy and the sparser QDOT surveys. Our reconstructions are based on the assumptions that cosmic structure has grown by gravitational instability and that fluctuations in the galaxy distribution are proportional to fluctuations in the mass distribution. We have paid particular attention to a careful estimation of random and systematic errors using a suite of mock PSCz catalogues constructed from large cosmological N-body simulations. As a further check on the validity of our results, we have implemented two independent methods for reconstructing the PSCz model velocity fields, both of which give consistent results.

Because of the large size of the PSCz survey, the density and velocity fields can be reliably reconstructed out to a depth of $150h^{-1}$ Mpc. We have presented maps of the galaxy distribution which, with a smoothing of $XS 6h^{-1}$ Mpc, clearly show the relative sizes of the main structures that characterize our local universe. The two largest peaks in our neighbourhood are the Great Attractor, made up of the Hydra–Centaurus and Pavo–Indus–Telescopium superclusters, and the Perseus–Pisces supercluster located in roughly opposite directions along the Supergalactic plane. The Local, Coma-A1367, and Camelopardalis superclusters as well as the Cetus Wall are clearly visible in our maps, as is the giant Shapley concentration which appears near the edge of the survey, behind the Great Attractor. The largest underdensity in our vicinity is the well-known Sculptor void, but this is almost matched in size by a void in the background of the Camelopardalis supercluster. Three more underdense regions that exert an important influence on the local dynamics are the voids in the foreground of Coma, in the background of the Perseus–Pisces complex, and behind the Great Attractor.

The local velocity field implied by the PSCz density field is complex. The dominant features are the organized infall patterns towards the large mass concentrations in the Great Attractor, Perseus–Pisces and Coma regions. Superimposed upon these are impressive coherent flows along a ridge between Cetus and Perseus–Pisces and along the Camelopardalis–Virgo–Great Attractor–Shapley direction. We see no prominent back-infall onto the Great Attractor. Instead, the flow in this region is a result of an interplay between the compressional push of two nearby voids and the pull of the Shapley concentration on much larger scales.

The PSCz reconstruction of the velocity field agrees well with results from the 1.2Jy survey within $80h^{-1}$ Mpc, the region in which the latter provides adequate sampling. The only noticeable difference are the predicted bulk velocity vectors which (in the CMB frame) differ in the two surveys by $\sim 130\beta$ km s $^{-1}$ in each Cartesian component. This discrepancy arises from uncertainties in the way in which the zone-of-avoidance is filled in and from the sampling noise of the density field at large distances. While the former affects the PSCz and 1.2Jy results equally, the latter is more severe in the 1.2Jy case because of the larger shot noise. Thus, the misalignment between the Local Group acceleration and the CMB dipole vectors is $\sim 25^\circ$ for the 1.2Jy survey, but only $\sim 15^\circ$ for the PSCz survey (Schmoldt *et al.* 1998). Comparison of the spherical harmonic multipoles of the two model velocity fields in radial shells confirms the consistency of the PSCz and 1.2Jy survey predictions in the region of overlap (Teodoro *et al.* 1998).

As was the case with the 1.2Jy survey, the velocity field reconstructed from the PSCz survey is partially inconsistent with the peculiar velocities in the Mark III catalogue. A visual inspection of the PSCz and 1.2 Jy velocity maps (Figs. 6 and 9) shows some differences around the Hydra–Centaurus complex, where the Mark III data exhibit a large shear, and in the Perseus Pisces region, which, in the Mark III catalogue, appears to participate in a large streaming motion (Davis, Nusser and Willick 1996). As pointed out by these authors, beyond $30 h^{-1}$ Mpc there is a large coherent residual dipole in the difference between the 1.2Jy gravity field and the Mark III peculiar velocity field. This cannot be ascribed to improper modelling of the gravity field by IRAS galaxies since the dipole depends only on the mass within the surveyed volume. Furthermore, Baker *et al.* (1998) have shown that the gravity field in the optical ORS survey (Santiago *et al.* 1995, 1996) is consistent with the 1.2Jy gravity field (and thus, by implication, with the PSCz field as well). This suggests that the undersampling of cluster cores by the predominantly spiral galaxy population in IRAS surveys does not have a large effect in the inferred gravity field. The most plausible explanation for the discrepancy between the Mark III velocities and the IRAS (and ORS) model predictions seems to be some systematic bias that affects the Mark III catalogue beyond $30 h^{-1}$ Mpc (Baker *et al.* 1998, Willick and Strauss 1998).

As we saw in §5.1, the density and velocity fields inferred from the PSCz survey agree well with those inferred from a sample of Abell/ACO clusters. This is perhaps surprising since clusters are selected in a very different way from galaxies, but it is reassuring and suggests that systematic errors are under control in both cases. Comparison of the two model density and velocity fields, smoothed on the same cubic grid, out to a distance of $140 h^{-1}$ Mpc, gives the relative linear bias, b_c , between the rich cluster population and PSCz galaxies. A simple χ^2 analysis of the density–density and velocity–velocity comparisons gives very similar results, $b_c = 4.4 \pm 0.6$ and $b_c = 4.7 \pm 0.6$, respectively. These values are consistent with the estimate, $b_c = 4.5$, obtained by Peacock and Dodds (1994) from an independent likelihood analysis of phenomenological power spectra. A more detailed comparison of the relative bias field of clusters and galaxies will be presented by Plionis *et al.* (1998).

Finally, averaging over the peculiar velocity field reconstructed from the PSCz survey, we have calculated the expected bulk velocity of concentric spheres around us. Comparison of these predicted bulk flows with those measured from the Mark III catalogue by Dekel *et al.* (1998) gives an estimate of $\beta = \Omega^{0.6}/b$. We implemented a likelihood analysis to carry out this comparison, taking into account the observed CMB dipole, the observed local shear field and the velocity of the Local Group predicted by the PSCz gravity field. If a high normalization for the power spectrum is assumed ($\sigma_8 = 0.87$), then our best estimate is $\beta = 0.6^{+0.22}_{-0.15} (1-\sigma)$. This value of β is consistent with results from analyses of the PSCz dipole (Schmoldt *et al.* 1998, Rowan–Robinson *et al.* 1998), and with the most recent determinations of β from velocity–velocity comparisons (Davis, Nusser & Willick 1996, Willick *et al.* 1997b, da Costa *et al.* 1998, Willick and Strauss 1998 and, within $1-\sigma$, also with Sigad *et al.* 1998). Adopting a low normalisation for the power spectrum gives a higher value of $\beta = 0.9^{+0.35}_{-0.20} (1-\sigma)$. While still consistent with most of the estimates above, such large values are only marginally consistent with the measured variance of the IRAS galaxy density field and the power spectrum normalization derived by Eke, Cole and Frenk (1996). Furthermore, with this normalization the bulk flows are also difficult to reconcile with the observationally favored values of Hubble’s constant, h , and the spectral shape parameter, Γ .

A more accurate determination of β , to 15% accuracy, is possible by performing a more detailed comparison

between the peculiar velocity field inferred from the PSCz survey and the measured peculiar velocities at independent locations. An analysis of this kind is currently in progress.

ACKNOWLEDGEMENTS

EB, LT and CSF thank Michael Strauss and Marc Davis for providing us with the original version of their reconstruction codes. The authors wish to thank Avishai Dekel for providing unpublished bulk velocity data and the referee, Michael Strauss, for many useful comments and suggestions. This work was supported by various PPARC grants and by the EC TMR network for research in “Galaxy formation and evolution.” LFAT was supported by a JNICT 's PRAXIS XXI PhD fellowship. CSF acknowledges a PPARC Senior Research Fellowship.

REFERENCES

- Abell G.O., 1958, ApJS, 3, 211
- Abell G.O., Corwin H.G., Olowin R.P., 1989, ApJS, 70, 1
- Babul A., Weinberg D., Dekel A., Ostriker J.P., 1994, ApJ, 427, 1
- Baker J., Davis M., Strauss M., Lahav O., Santiago B., 1998 astro-ph/9802713/
- Baugh, C., 1996, MNRAS, 280, 267
- Beichman,C.A., Neugebauer,G., Habing,H.J., Clegg,P.E., Chester,T.J. 1988. in IRAS catalogs and atlases, Volume 1; Explanatory supplement (JPL).
- Branchini E., Plionis M., 1996, ApJ, 460, 569 [BP96]
- Branchini, E., Plionis, M. Zehavi, I., Dekel, A., 1997, MNRAS, *submitted*
- Branchini, E., Teodoro, L. Schmoltdt, I., Frenk, C., Efstathiou, G., 1998, *in preparation*
- Brown, M., Peebles P. 1987, ApJ, 317, 588
- Cole, S., 1997, MNRAS, 286, 38
- Cole, S., Hatton, S., Weinberg, D., and Frenk C. 1998, astro-ph/980125
- Davis M., Peebles P.J.E., 1985, ARA&A, 21, 109
- Davis M., Strauss M.A., Yahil A., 1991, ApJ, 372, 394
- Davis M., Nusser, A., Willick J. 1997, ApJ 473, 22
- da Costa L., Freudling W., Wegner G., Giovanelli R., Haynes M., Salzer J., 1996, ApJ, 468, L5
- da Costa L., Nusser A., Giovanelli R., Haynes M., Salzer J., Wegner G., 1998, MNRAS, 299, 425
- Davis, M., Efstathiou, G., White, S., and Frenk, C. 1985, ApJ 292,371
- Davis M., Nusser, A., Willick J. 1997, ApJ, 473, 22
- Dekel A., Bertschinger E., Faber S.M., 1990, ApJ, 364, 349
- Dekel A., Bertschinger E., Yahil A., Strauss M., Davis M., Huchra J., 1993, ApJ, 412, 1
- Dekel A., 1994, ARA&A, 32, 371
- Dekel, A, 1997, in da Costa L.N., Renzini A., eds, Galaxy Scaling Relations. Springer, p. 245
- Dekel A., Eldar A., Kolatt T., Yahil A., Willick J., Faber S., Courteau S., Burstein D., 1998, *preparation*
- de Vaucouleurs G. 1953, Aj, 58, 30
- Eke, V., Cole, S., and Frenk, C. 1996, MNRAS 282, 263
- Eldar, A., *et al.* 1998 *in preparation*
- Fisher K., Huchra J.P., Strauss M., Davis M., Yahil A., Schlegel D., 1995a, ApJS, 100, 69.
- Fisher K., Lahav O., Hoffman Y., Lynden–Bell D., Zaroubi S., 1995b, MNRAS, 272, 885.
- Freudling W., da Costa L., Pellegrini P. S., 1994, MNRAS, 268, 943
- Giovanelli R., Haynes M., Herter T., Vogt N., Wegner G., Salzer J., da Costa L., Freudling W., 1997a, AJ, 113, 22
- Giovanelli R., Haynes M., Herter T., Vogt N., da Costa L., Freudling W., Salzer J., Wegner G., 1997b, AJ, 113, 53
- Giovanelli R., Haynes M., Freudling W., da Costa L., Salzer J., Wegner G., 1998a, astro-ph/9807274
- Giovanelli R., Haynes M., Salzer J., Wegner G., da Costa L., Freudling W., 1998b, astro-ph/9807274
- Guzzo, L., Strauss, M., Fisher K., Giovanelli, R., and Haynes M. 1997, ApJ, 489, 37
- Han M., Mould J., 1990, ApJ, 360, 448.
- Hermit S., Santiago B. S., Lahav O., Strauss M., Davis M., Dressler A., Huchra J.P., 1996, MNRAS, 283, 709
- Hudson M.J., 1994, MNRAS, 266, 475
- Hudson M., Dekel A., Courteau S., Faber S.M., Willick J.A., 1995, MNRAS, 274, 305
- Hudson M., Smith R., Lucey J., Schlegel D., Davis R., 1998 in proc. of MPA/ESO workshop 'Evolution of Large Scale Structure' *in press*
- Jenkins A., Frenk C. S., Pearce F. R., Thomas A. P., Colberg J. M., White S.D.M., Couchman H.M.P., Peacock J. A., Efstathiou G., Nelson A. H., 1998, ApJ, 499, 20
- Kaiser N., 1988, MNRAS, 231, 149
- Kaiser N., and Lahav, O., 1989, MNRAS, 237, 129
- Kaiser N., Efstathiou G., Ellis R., Frenk C., Lawrence A., Rowan–Robinson M., Saunders W., 1991, MNRAS, 252, 1
- Kolatt T., Dekel A., Ganon G., Willick J.A., 1996, ApJ, 458, 419
- Lauer T., Postman M., 1994, ApJ, 425, 418 [LP94]
- Lynden–Bell D., Faber S.M., Burstein D., Davies R., Dressler A., Terlevich R., Wegner G., 1988, ApJ, 326, 19
- Moshir M., Kopan G., Conrow T., McCallon H., Hacking P., Gregorich,D., Rohrbach G., Melynk M., Rice,W., Fullmar L., White,J., Chester T. 1989. in IRAS Faint Source Survey Catalog, Version 1. (Washington, DC:GPO)(FSSC)
- Nusser A., Davis M., 1994, ApJ, 421, 1L
- Peacock J. A., Dodds S. J., 1994, MNRAS, 267, 1020
- Peebles P.J.E., 1980, The Large Scale Structure of the Universe, Princeton University Press, Princeton

- Peebles P.J.E., 1988, ApJ, 332, 17
- Plionis M., *et al.* 1998 *in preparation*
- Riess A., Press W., Kirschner R., 1995, ApJ, 438, L17
- Rowan-Robinson M., Lawrence A., Saunders W., Crawford J., Ellis R., Frenk C.S., Parry I., Xiaoyang X., Allington-Smith, J., Efstathiou G., Kaiser N., 1990, MNRAS, 247, 1
- Santiago, B. X., Strauss, M., Lahav, O., Dressler, A., and Huchra, J., 1995, ApJ, 446, 457
- Santiago, B. X., Strauss, M., Lahav, O., Davis, M., Dressler, A., and Huchra, J., 1996, ApJ, 461, 38
- Saunders W. *et al.* 1998a, in Proc. of the XXXII Moriond Astrophysics Meeting. *in press*
- Saunders W. *et al.* 1998b, *in preparation*
- Scaramella R., 1995, Aatr. Lett. and Comm., 32, 137
- Schmoldt I., 1988, MNRAS, *submitted*
- Shaya E., Tully B., Pierce M., 1992, ApJ, 391, 16
- Sigad Y., Dekel A., Strauss M., Yahil A., 1998, ApJ, 495, 516
- Springel V. 1996, Topology and Luminosity Function of the PSCz Redshift Survey, M.Sc. Thesis, Eberhard-Karls-Universität Tübingen
- Springel V., White S.D.M. 1998, MNRAS, *in press*
- Strauss M., Davis M., 1988, in Rubin V.C., Coyne G., eds, Large Scale Motions in the Universe: A Vatican Study Week. Princeton Univ. Press, Princeton, p. 255
- Strauss M.A., Davis M., Yahil A., Huchra J.P., 1990, ApJ, 361, 49
- Strauss M.A., Davis M., Yahil A., Huchra J.P., 1992a, ApJ, 385, 421
- Strauss M.A., Yahil A., Davis M., Huchra J.P., Fisher K., 1992b, ApJ, 397, 395
- Strauss M.A., Cen R.Y., Ostriker J.P., Lauer T.R., Postman M., 1995, ApJ, 446, 507
- Strauss M.A., Willick J.A., 1995, Phys Rep., 261, 271
- Strauss, M., 1997, in N. Turok ed., Critical Dialogues in Cosmology, World Scientific, p.423.
- Strauss M.A., Ostriker, J., Cen, R. 1998, ApJ, 493,39
- Tadros H., Ballinger W. E., Taylor A. N., Heavens A. F., Efstathiou G., Saunders W., Frenk C.S., Keeble O., McMahon R., Maddox S. J., Oliver S., Rowan-Robinson M., Sutherland W.J., White S.D.M. 1998, MNRAS, *submitted*
- Teodoro L., *et al.* 1998 *preparation*
- Tormen G., Bertschinger E., 1996, ApJ., 472, 14
- Tully B., 1997, Nearby Galaxy Catalog, Cambridge University Press
- Watkins R., Feldman H., 1995, ApJ, 453, 73
- Webster M., Lahav O., Fisher K., 1997, MNRAS, 287, 425
- Willick J., Courteau S., Faber S., Burstein D., Dekel A., Strauss M., ApJS, 1997a, 109, 333.
- Willick, J., Strauss, M., Dekel, A., and Kolatt, T. 1997b, ApJ, 486, 629
- Willick, J., and Strauss, M. 1998, astro-ph/9801307
- Yahil A., Strauss M.A., Davis M., Huchra J.P., 1991, ApJ, 372, 380

Table 1. Parameters for the selection function of IRAS Galaxies

Sample	α	β	r_s	r_*	$l(100)$	$\langle n \rangle$
z-IRAS PSCz	0.54	1.83	6.0	87.00	11.67	$5.76 \cdot 10^{-2}$
R-IRAS PSCz	0.52	1.92	6.0	90.75	11.66	$4.61 \cdot 10^{-2}$
z-IRAS 1.2Jy	0.49	1.80	6.0	51.27	16.21	$6.41 \cdot 10^{-2}$
R-IRAS 1.2Jy	0.47	1.87	6.0	52.50	16.24	$5.51 \cdot 10^{-2}$

Table 2. Parameters for the selection function of Abell/ACO clusters

Sample	r_{c1}	r_{c2}	r_{c1}	r_{c2}	A_1	A_2	$\langle n \rangle$
Abell/ACO	31.8	44.0	180	235	125	289	$4.61 \cdot 10^{-5}$

Table 3. The cluster/IRAS galaxy relative bias parameter, b_c . The top and bottom rows give results with and without applying the cluster collapsing procedure. Column 1: N_t^δ , the number of gridpoints used for the regression analysis; column 2: $N_{d.o.f.}$, the number of independent volumes; column 3: b_c^δ from the δ - δ regression and its 1- σ error; column 4: A_δ , the zero point offset in the δ - δ regression and its 1- σ error; column 5: $S^\delta = \chi_{eff}^2 / N_{dof}$ from the δ - δ regression; column 6: b_c^δ from the v_y - v_y regression and its 1- σ error; column 7: A^{v_y} , the zero point offset in the v_y - v_y regression and its 1- σ error; column 8: $S^{v_y} = \chi_{eff}^2 / N_{dof}$ from the v_y - v_y regression.

N_t	$N_{d.o.f.}$	b_c^δ	A^δ	S^δ	$b_c^{v_y}$	A^{v_y}	S^{v_y}
6427	54	4.4 ± 0.6	0.06 ± 0.07	1.14	4.7 ± 0.6	-16 ± 90	1.55
6527	55	4.5 ± 0.6	0.12 ± 0.07	1.15	4.6 ± 0.6	8.2 ± 91	1.57

FIGURE CAPTIONS

Figure 1. Aitoff projection of the galaxy distribution in galactic coordinates, in the PSCz survey (upper panel) and in a mock catalogue constructed from a cosmological cold dark matter N-body simulation (lower panel). The filled-in regions show unobserved or obscured regions; the zone-of-avoidance is the quasi-horizontal strip surrounding the galactic plane.

Figure 2. Lower Plot: the number of galaxies as a function of redshift-distance in the PSCz (upper histogram) and 1.2 Jy (lower, shaded histogram) samples. The curves show the expected counts as a function of distance estimated from the selection functions. The heavy line at the bottom shows the predicted distance distribution of Abell/ACO clusters. The labels give the total number of objects in each sample. Upper plot: the ratio between the observed and the expected number of galaxies in the PSCz catalogue (thick line) and in the IRAS 1.2 Jy catalogue (thin line).

Figure 3. Mean inter-object separation as a function of radial distance (in h^{-1} Mpc) in the three samples considered in this paper: PSCz galaxies (continuous line), 1.2 Jy galaxies (dashed line) and Abell/ACO clusters (dot-dashed line).

Figure 4. Two dimensional slices through the density and velocity fields in a mock PSCz catalogue, corresponding to the mock Supergalactic plane. The hypothetical observer is located in a region analogous to the Local Group. Data are shown in a sphere of radius $120h^{-1}$ Mpc centred on the observer. Both density and velocity fields have been smoothed using a Gaussian filter of radius $6 h^{-1}$ Mpc. The upper left-hand plot shows the true fields while the upper plot on the right shows the reconstructed fields using Method 1. Continuous lines represent isodensity contours with a spacing of 0.5 in δ . Solid lines encompass overdensities and dashed lines underdensities. The heavy line indicates the $\delta = 0$ contour level. The amplitude of the velocity vectors is on an arbitrary scale. In the lower left-hand plot we show the error map for the density field. Contours for the absolute value of the discrepancy between overdensities, Δ , are drawn at steps of 0.25. The shaded region around SGY=0 is the mock zone-of-avoidance. The lower plot on the right shows the difference between the true and reconstructed velocity fields.

Figure 5. Real space density field derived from the PSCz survey. A slice along the Supergalactic plane is shown. The field has been smoothed with a variable Gaussian filter. The smoothing length is set at a constant value of $3h^{-1}$ Mpc within $30h^{-1}$ Mpc and increases linearly with distance up to a value of $11.25h^{-1}$ Mpc at $150 h^{-1}$ Mpc, where the most distant structure are located. The yellow line shows the $\delta = 0$ contour.

Figure 6. Real space density and velocity fields derived from the PSCz survey. The fields, smoothed with with a $6h^{-1}$ Mpc Gaussian are shown in a slice along the Supergalactic plane. The most distant structures are located at $80h^{-1}$ Mpc. The thick continuous line shows the $\delta = 0$ contour. Positive (continuous lines) and negative (dashed lines) contours are plotted at steps of $\Delta\delta = 0.5$. The amplitude of the velocity vectors, obtained for $\beta = 1$, is on an arbitrary scale. This reconstruction has been performed using Method 1.

Figure 7. The same fields as in Fig. 6, but in two slices parallel to the Supergalactic plane. The top panels refer to the slice at SGZ= $+40 h^{-1}$ Mpc, above the Supergalactic plane, while the ones at the bottom refer to the slice at SGZ= $-40 h^{-1}$ Mpc, below the galactic plane. Density and velocity fields are plotted separately following the same conventions adopted in Fig. 6. This reconstruction has been performed using Method 1 for a value of $\beta = 1$.

Figure 8. The peculiar velocity field reconstructed using Method 1 (top left panel) and Method 2 (top right panel), smoothed with a $6 h^{-1}$ Mpc Gaussian in a slice along the Supergalactic plane. The amplitude of the velocity vectors is on the same arbitrary scale in the two panels. The lower panel is a scatter plot of the SGY components of the velocity vectors illustrated in the upper panels. Only 1000 points, randomly selected from the ones within $80 h^{-1}$ Mpc, have been plotted. The parameters of the linear fit (A,B) are indicated in the legend, along with the scatter in the model velocities (σ).

Figure 9. The same as Fig. 6 but the density and velocity fields have been derived from the 1.2Jy survey. This reconstruction has been performed using Method 1.

Figure 10. Map of the difference between the density and velocity fields obtained from the PSCz and the 1.2 Jy catalogues in a slice along the Supergalactic plane. The lower panel shows the difference between the two overdensity fields, $\Delta = \delta_{PSCz} - \delta_{1.2Jy}$: positive (continuous lines) and negative (dashed lines) isodensity contours are drawn at

steps of $\Delta\Delta = 0.25$; a thick line connects the points in which $\Delta = 0$. The difference between the two velocity fields, both obtained for $\beta = 1$, is displayed in the upper panel. The amplitude of the velocity vectors is on an arbitrary scale.

Figure 11. Point-by-point comparison of the 1.2Jy and PSCz density and velocity fields within $80 h^{-1}$ Mpc. Only the values at 1000 randomly chosen gridpoints are plotted. The upper panel shows a velocity–velocity scatter plot for the SGY components of the peculiar velocity (assuming $\beta = 1$). The lower panel shows the δ – δ comparison. The parameters of the linear regression fit are given in both panels.

Figure 12. A section, along the Supergalactic plane, through the real space density and velocity fields derived from the PSCz survey. The fields have been smoothed with a $6h^{-1}$ Mpc Gaussian. This figure is similar to Fig. 6, except that it displays data in a larger spherical volume of radius $120h^{-1}$ Mpc. The thick continuous line is the $\delta = 0$ contour. Positive (continuous lines) and negative (dashed lines) contours are plotted at steps of $\Delta\delta = 0.5$. The amplitude of the velocity vectors is on an arbitrary scale. This reconstruction has been performed using Method 1.

Figure 13. Four slices, parallel to the Supergalactic plane, through the same density model illustrated in Fig. 12. The different panels refer to slices at $SGZ=+40, +80, -40$ and $-80 h^{-1}$ Mpc, respectively. The same conventions as in Fig. 6 are adopted.

Figure 14. PSCz velocity fields corresponding to the density fields of Fig. 13. The amplitude of the velocity vectors is on an arbitrary scale.

Figure 15. Real space density fields derived from the PSCz survey (upper panel) and Abell/ACO clusters (lower panel) within a distance of $140 h^{-1}$ Mpc. Both fields have been smoothed with a $20h^{-1}$ Mpc Gaussian. Here we show a slice along the Supergalactic plane. The $\delta = 0$ level is indicated by the thick line. Other contours are plotted in steps of $\Delta\delta = 0.2$ for the PSCz map and $\Delta\delta = 0.88$ for the clusters map. The dashed lines delineate the zone-of-avoidance in each sample.

Figure 16. Cluster (left) and PSCz (right) density fields, as in Fig. 15, but in four slices along the Supergalactic plane, at $SGZ=+100,+45,-45,-100 h^{-1}$ Mpc. The level of the density contours is also as in Figure 15.

Figure 17. Peculiar velocity fields derived from the PSCz survey (upper panel) and Abell/ACO clusters (lower panel) corresponding to the density fields in Fig 15. Both fields have been smoothed with a $20h^{-1}$ Mpc Gaussian. The amplitude of the velocity vectors is on an arbitrary scale, but the cluster field has been scaled according to a relative bias parameter, $b_c = 4.4$. The dashed lines delineate the zone-of-avoidance in each sample.

Figure 18. Error maps similar to the one displayed in Figure 4, except that a different mock PSCz catalogue is used and a larger Gaussian smoothing of $20 h^{-1}$ Mpc is assumed. The density contours are drawn at steps of $\Delta\Delta = 0.1$ in the upper plots and of $\Delta\Delta = 0.05$ in the lower left–hand plot.

Figure 19. Density and velocity scatterplots for the reconstructions based on the PSCz survey and a sample of Abell/ACO clusters. For clarity only ~ 1000 out of 1878 gridpoints within a sphere of radius $120h^{-1}$ Mpc, and lying within $|b| \geq 20^\circ$, are plotted. The velocity–velocity comparison in the upper panel refers to the SGY–component. The lower panel shows the δ – δ comparison. The parameters in the legend refer to the χ^2 fits discussed in the text (see also Table 3). The errorbars give the mean $1-\sigma$ errors in the two model fields.

Figure 20. Random and systematic errors in the model bulk flow derived from the analysis of mock PSCz catalogues. The upper panel shows the difference between the true cumulative bulk velocity vector and the vector reconstructed using Method 1. Different symbols are used for the three Cartesian components, as indicated in the figure. The lower panel shows the ratio between the amplitudes of the reconstructed and true bulk flow vectors (filled circles) and their SGY Cartesian components (open circles).

Figure 21. The amplitude (upper left-hand plot) and the direction (upper right-hand plot) of the cumulative bulk velocities predicted in different models. The circles give results from the PSCz survey using Method 1 (open circles) and Method 2 (filled circles); the filled squares give results from the 1.2Jy survey using Method 1; the triangles give results from the Abell/ACO cluster sample. For the models based on IRAS galaxies, the amplitudes have been normalized to $\beta = 1$, while for the cluster model the velocities have been normalized assuming a relative bias, $b_c = 4.4$. The errorbars give $1-\sigma$ uncertainties obtained from the PSCz survey using Method 1. The dot–dashed line shows the

PSCz reconstruction using Method 1, statistically corrected to minimise the volume bias. The right-hand panel gives the direction of the predicted cumulative bulk flow at $60 h^{-1}$ Mpc in galactic coordinates (l, b) . The asterisk at the centre marks the direction of the CMB dipole and the different samples are indicated by the same symbols used in the top left-hand plot. Errorbars are $1\text{-}\sigma$ uncertainties derived from the analysis of the mock catalogues. The contours are set at constant misalignment angle from the apex of the CMB dipole, in steps of $\Delta\theta = 10^\circ$. The lower plot shows the misalignment angle between the various model bulk flows as a function of distance. The difference angle between models M1 and M2 (continuous line), M1 and 1.2 Jy (short dashed line) and M1 and Clusters (short dashed line) is displayed.

Figure 22. The amplitude (left) and direction (right) of the cumulative bulk velocity vector. The bottom-left panel refers to the total velocity and the top-left panel to the SGY-component only. The filled triangles show the bulk velocity measured from the Mark III catalogue by Dekel *et al.* (1998) and the filled square the bulk velocity measured from the SFI catalogue by Eldar *et al.* (1998). The open triangle shows the bulk flow inferred from a survey of 44 Type Ia supernovae by Riess, Press & Kirshner (1995). The open square gives the bulk velocity derived by Lauer & Postman (1994) from a survey of brightest cluster galaxies. The dot-dashed lines bracket the $1\text{-}\sigma$ range of the bulk velocity predicted from the PSCz gravity field using Method 1, and corrected for the effects of long-wavelength modes. In the both panels the model predictions are normalized to $\beta = 0.75$. In the right-hand panel, the asterisk marks the direction of the CMB dipole in galactic coordinates and the filled circle the direction of the bulk velocity at $50h^{-1}$ Mpc obtained from the PSCz survey using the corrected Method 1. The other symbols correspond to those in the left-hand panel, at a distance of $50 h^{-1}$ Mpc in the case of the Mark III catalogue.

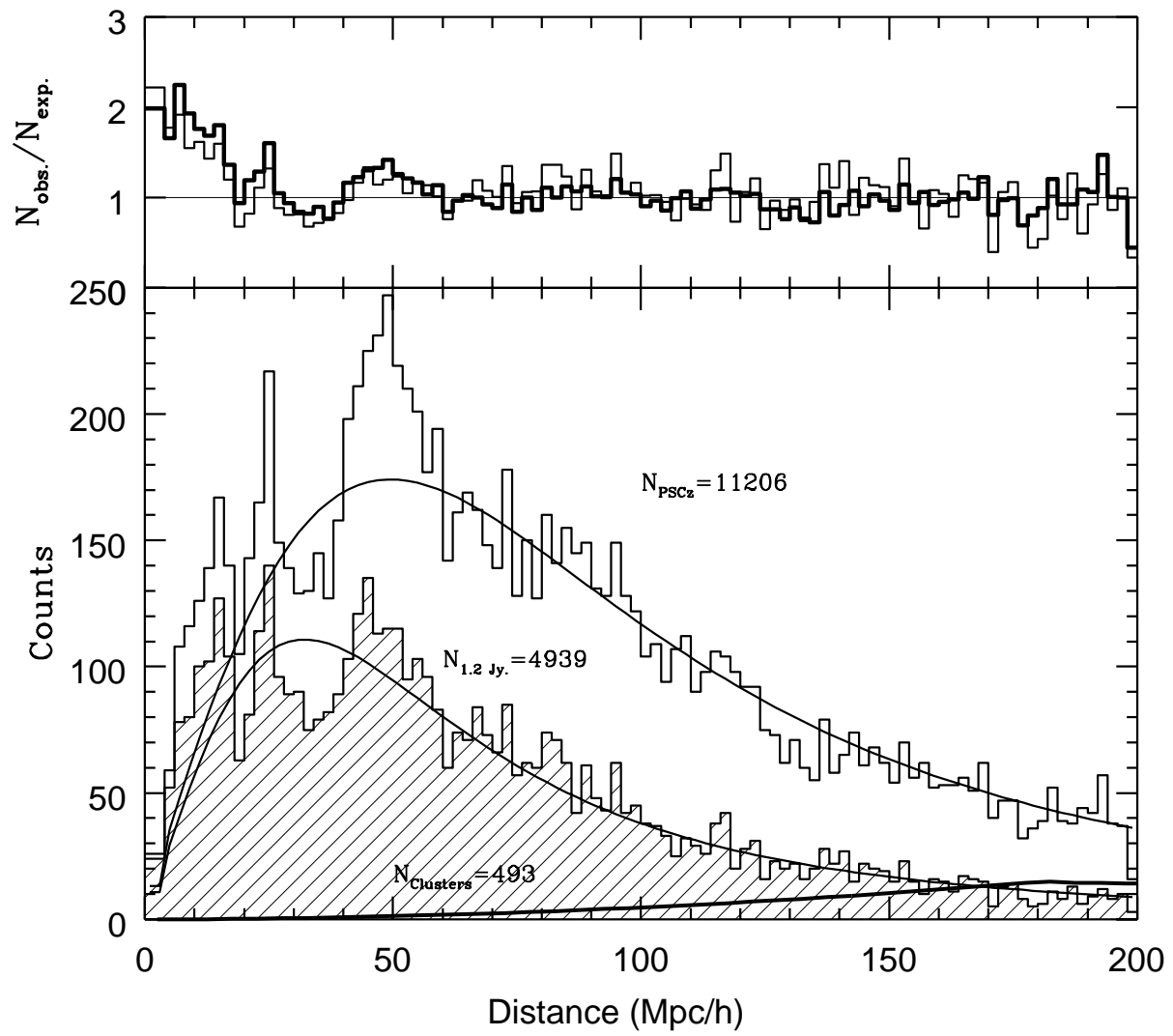
Figure 23. Likelihood contours of $\mathcal{L}(\mathbf{v}_M(i), i = 1, 4; \mathbf{v}_P(j), j = 1, 8)$ in the $\beta, l_{eq} = 1/\Gamma$ plane. The minimum (or the minima) is displayed by a small horizontal line. The left-hand panel assumes $\sigma_8 = 0.87$ and the right-hand panel $\sigma_8 = 0.52$. The vertical lines encompass the range for which $0.4 < h < 0.8$, for $\Omega = 1$ in the left panel and $\Omega = 0.3$ in the right panel.

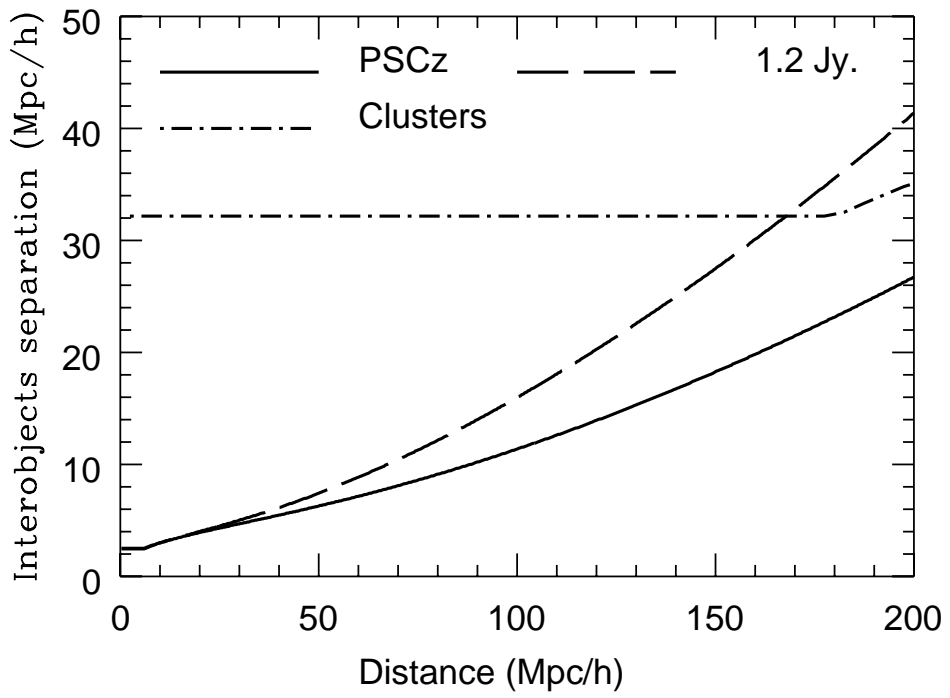
Figure 24. As Fig. 23 but the contours displayed here refer to the conditional likelihood function $\mathcal{L}(\mathbf{v}_M(i), i = 1, 4; \mathbf{v}_P(j), j = 1, 8; \mathbf{v}_d(k), k = 1, N; \mathbf{v}_{LG}|\mathbf{v}_s)$.

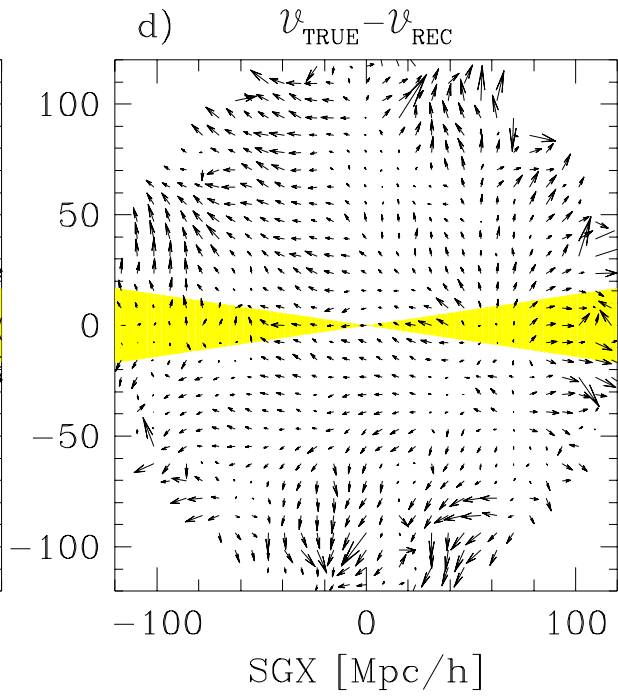
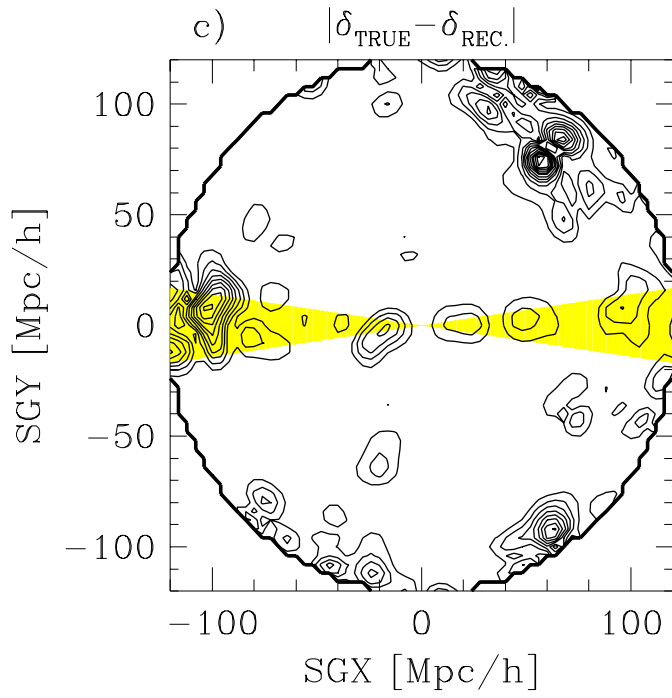
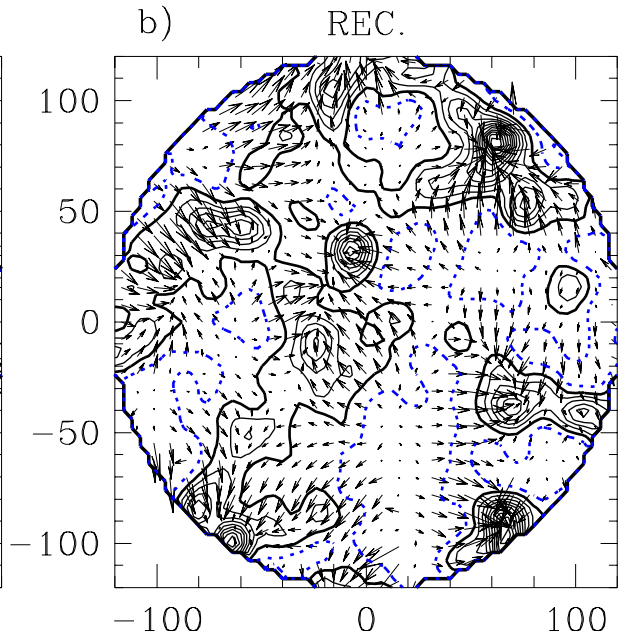
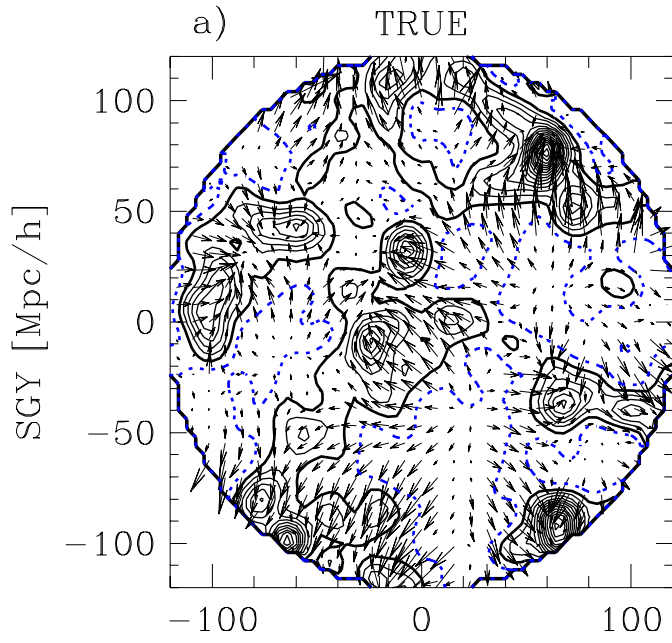
Figure 25. Marginal distributions of the likelihood of β for $\sigma_8 = 0.87$ (left panel) and $\sigma_8 = 0.52$ (right panel). Continuous lines give the result of integrating over all values of Γ , while dot dashed lines give the results of limiting the integration to the range encompassed by the vertical lines in Fig. 24.

This figure "fig1.gif" is available in "gif" format from:

<http://arxiv.org/ps/astro-ph/9901366v2>

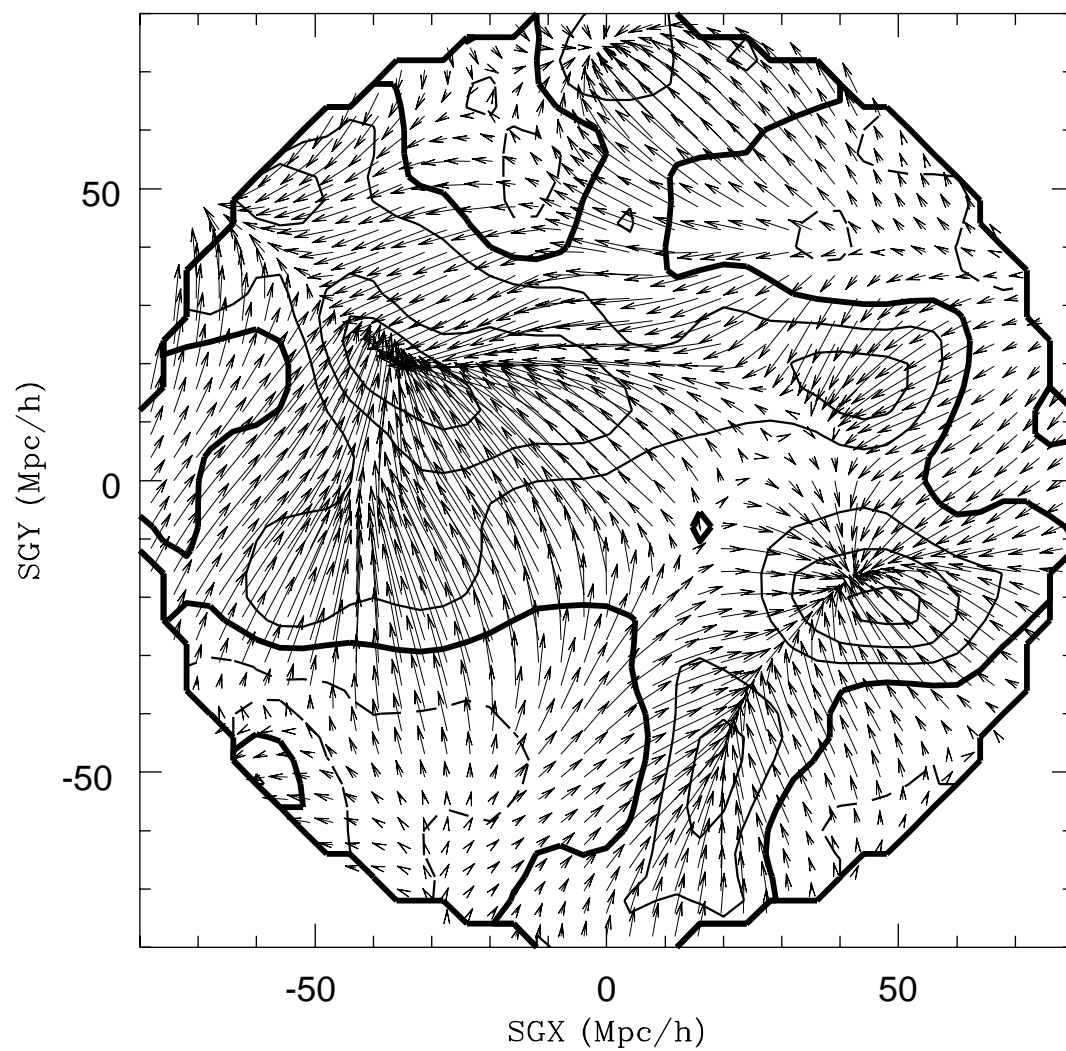




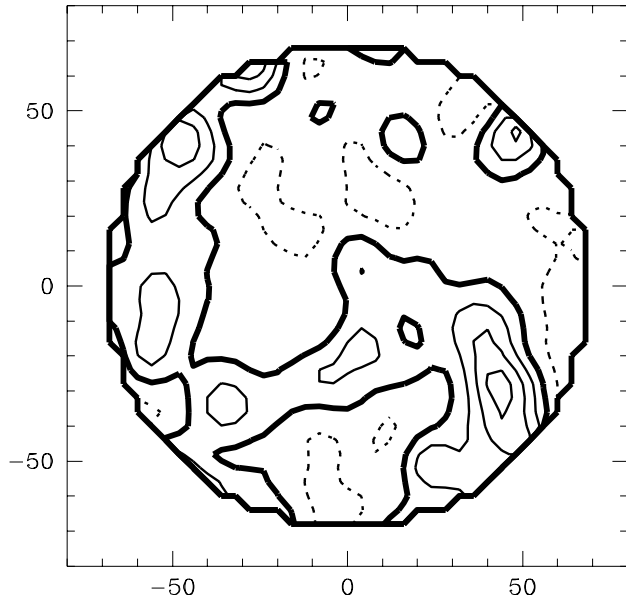
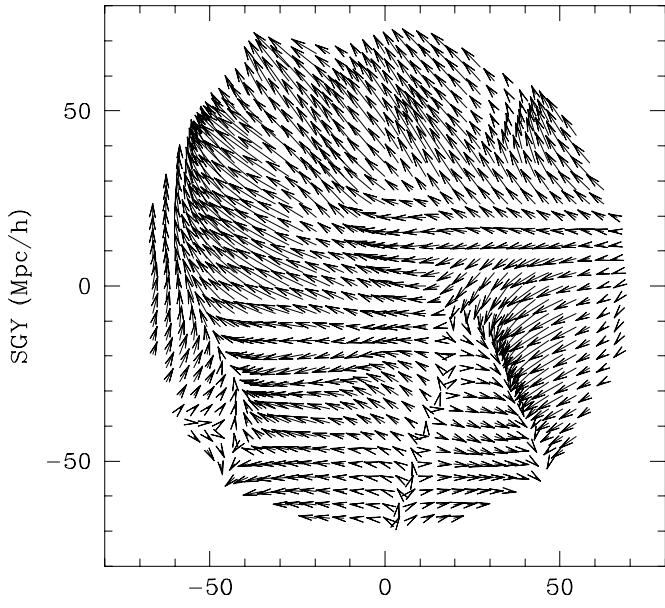


This figure "fig5.gif" is available in "gif" format from:

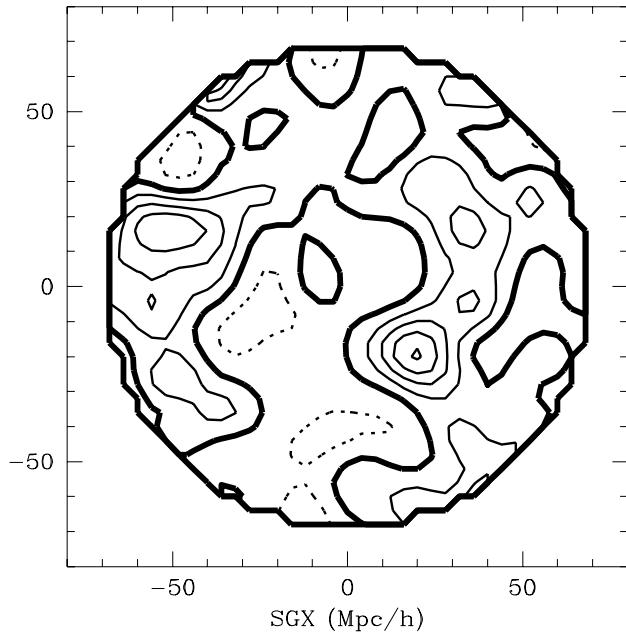
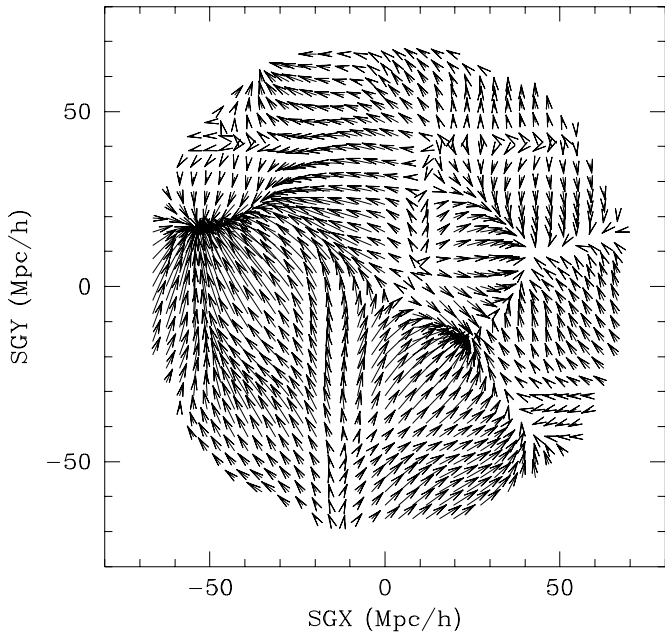
<http://arxiv.org/ps/astro-ph/9901366v2>



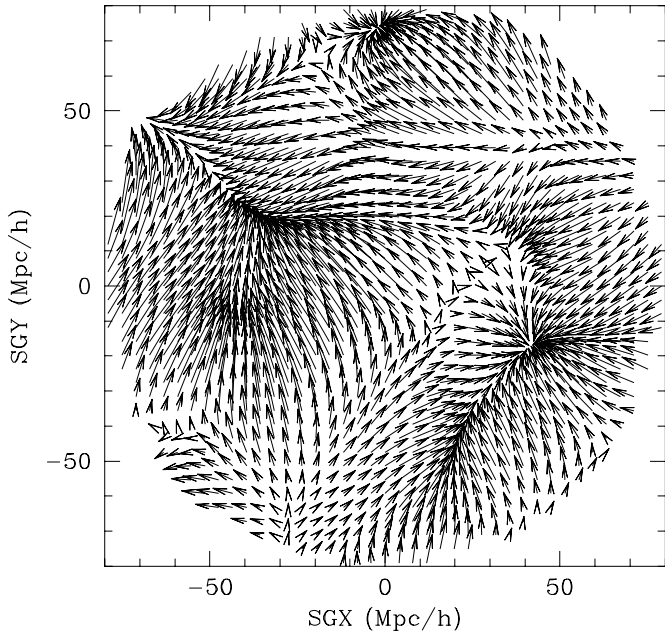
SGZ=+40



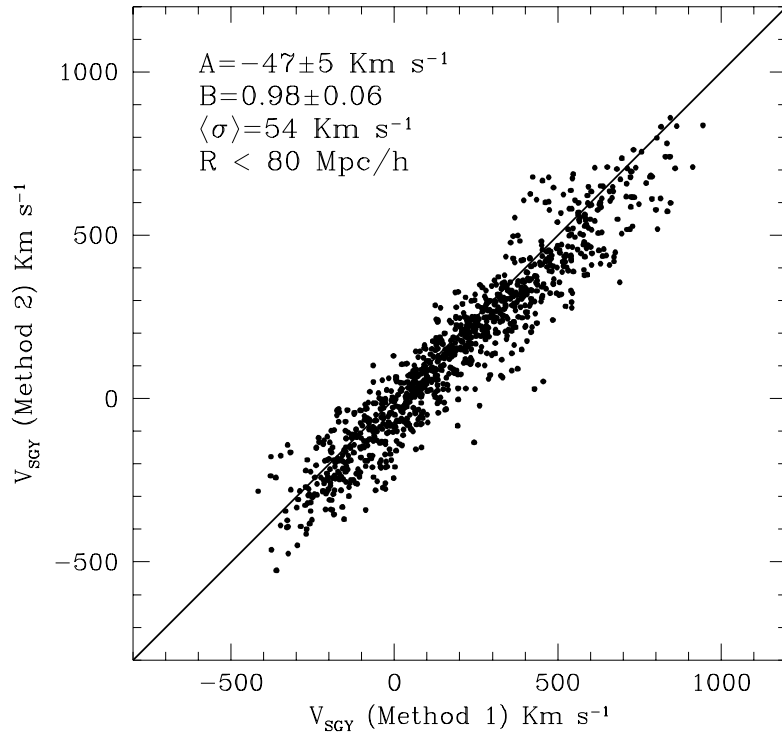
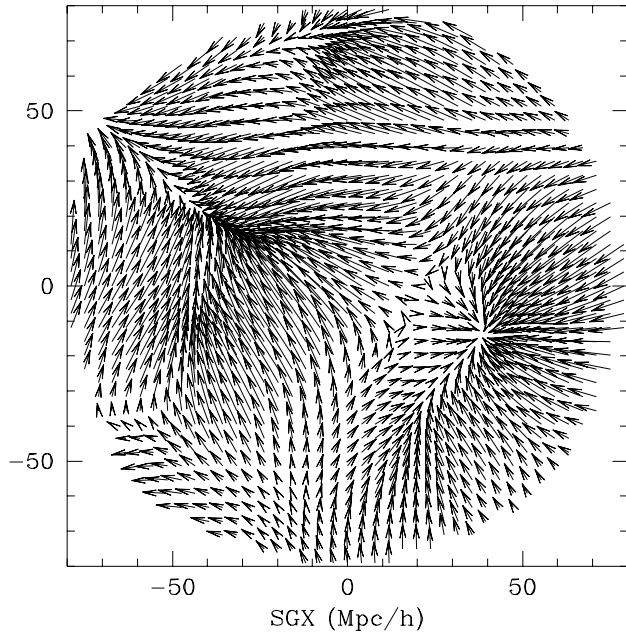
SGZ=-40

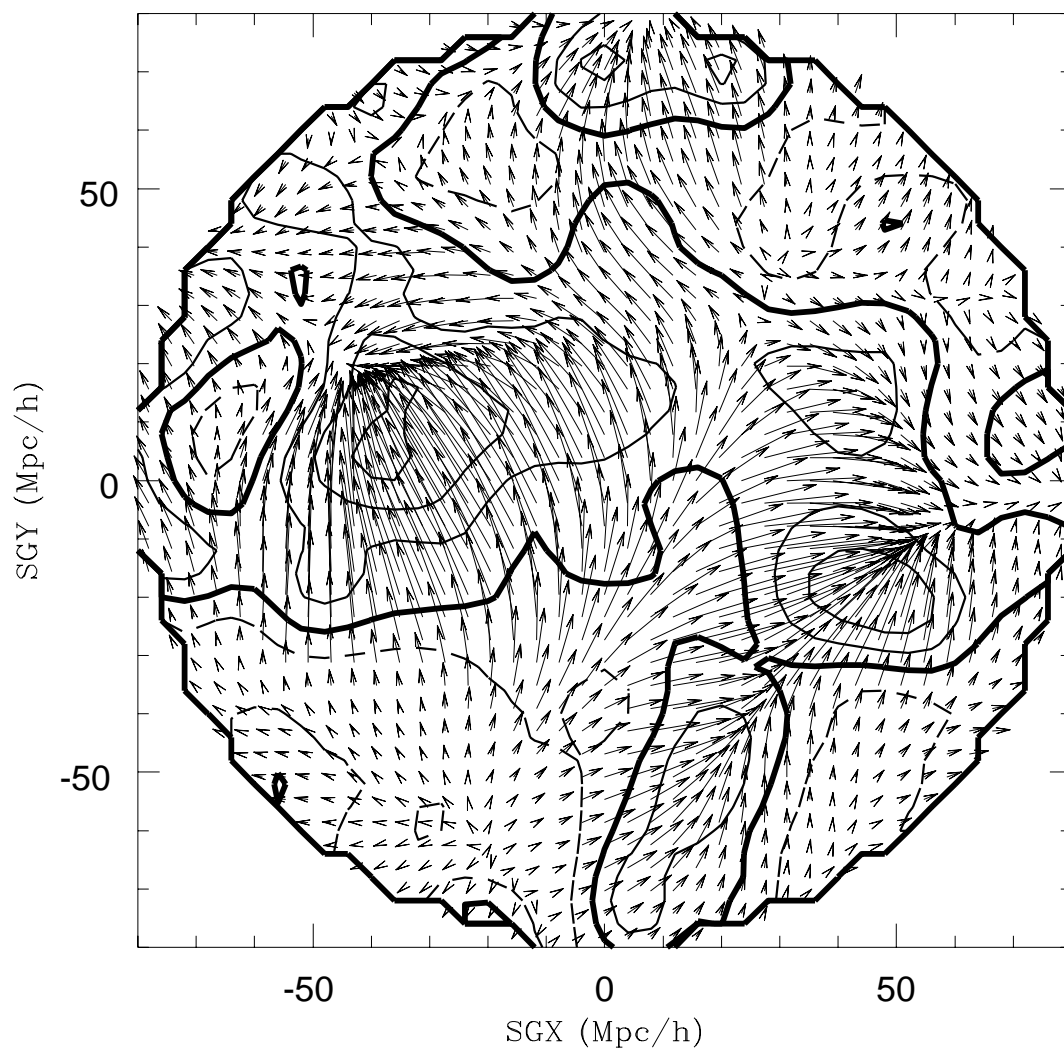


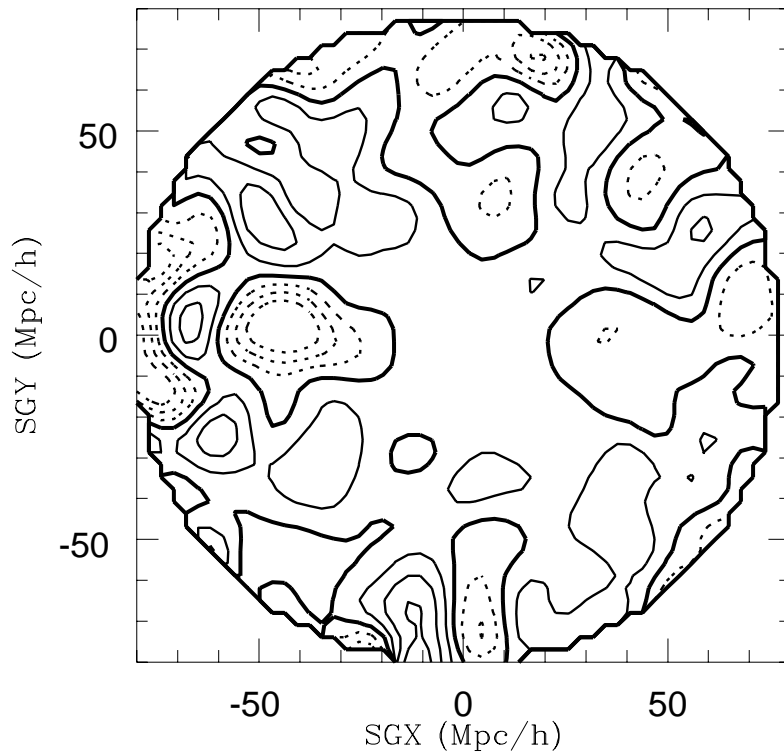
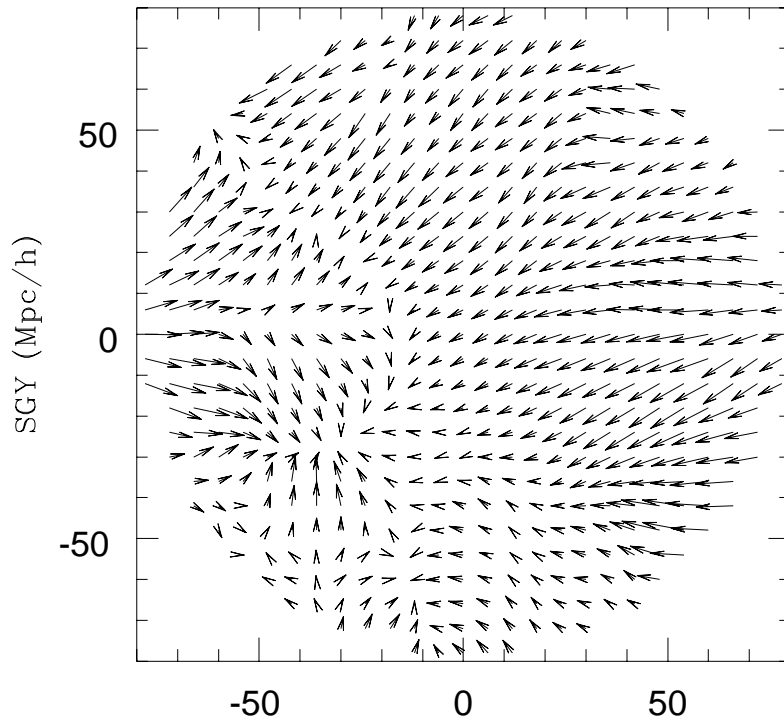
Method 1

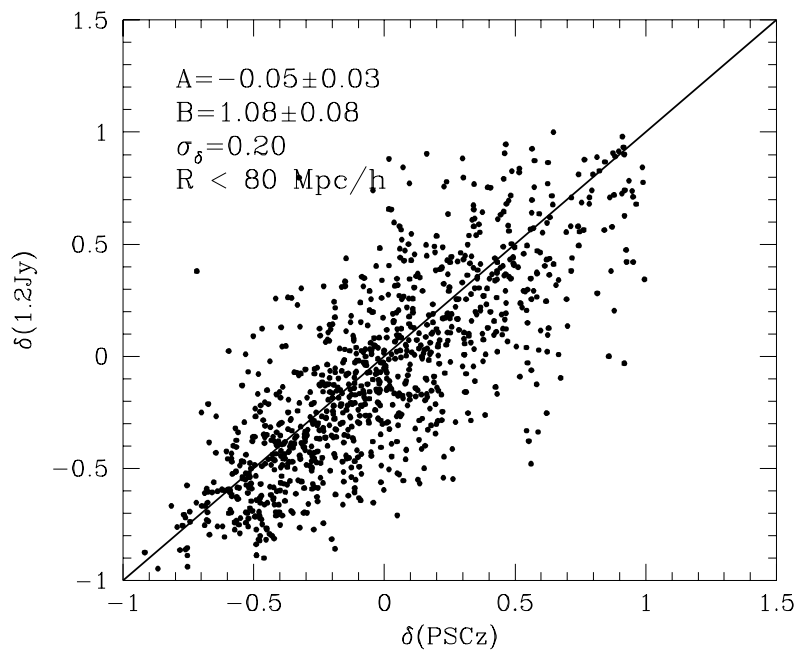
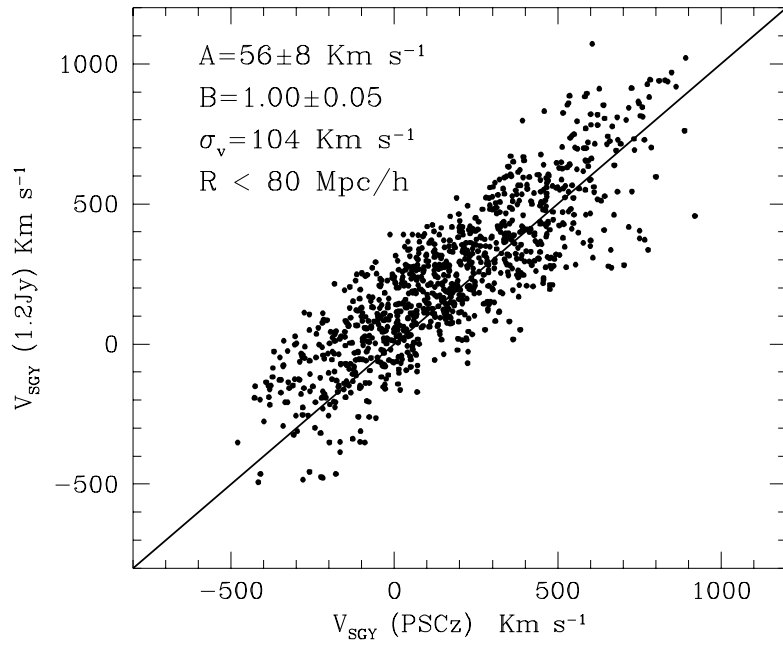


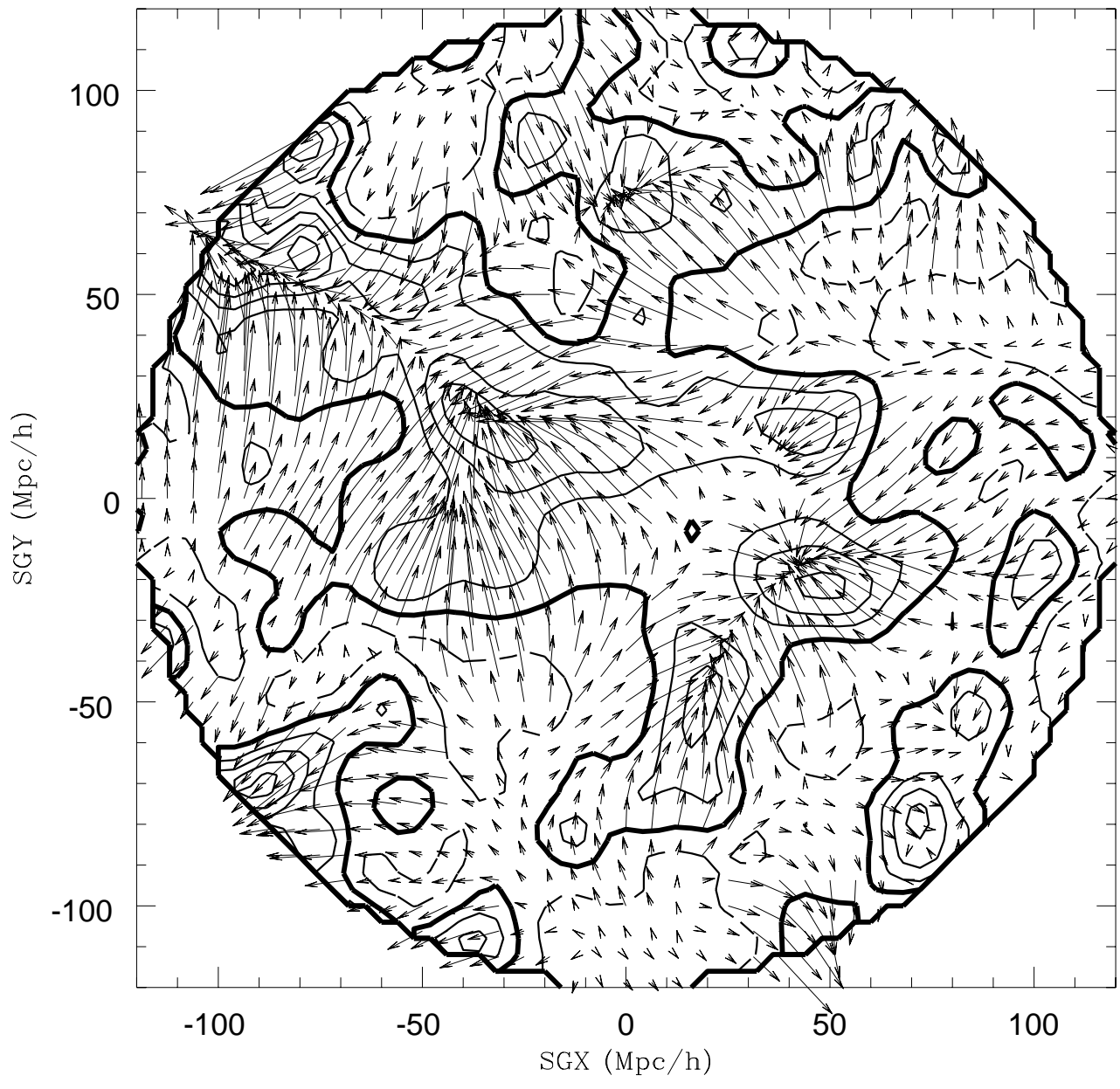
Method 2



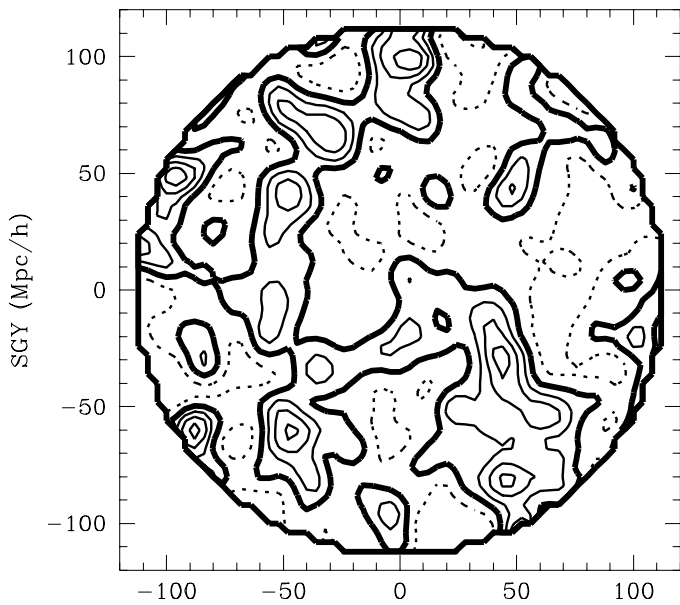




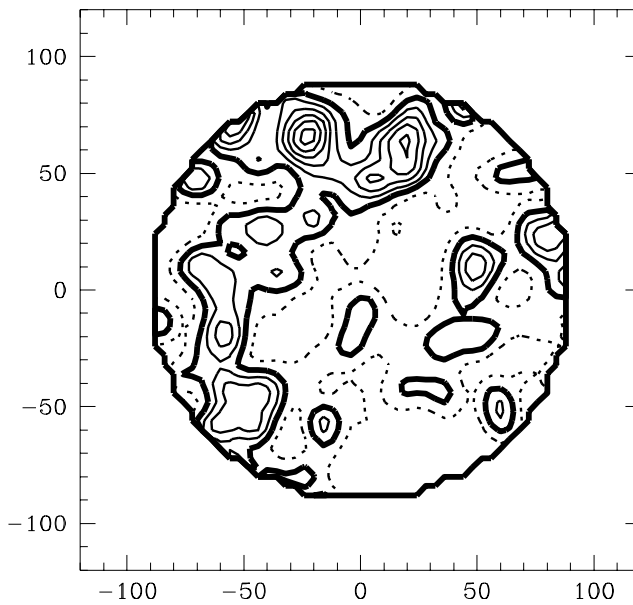




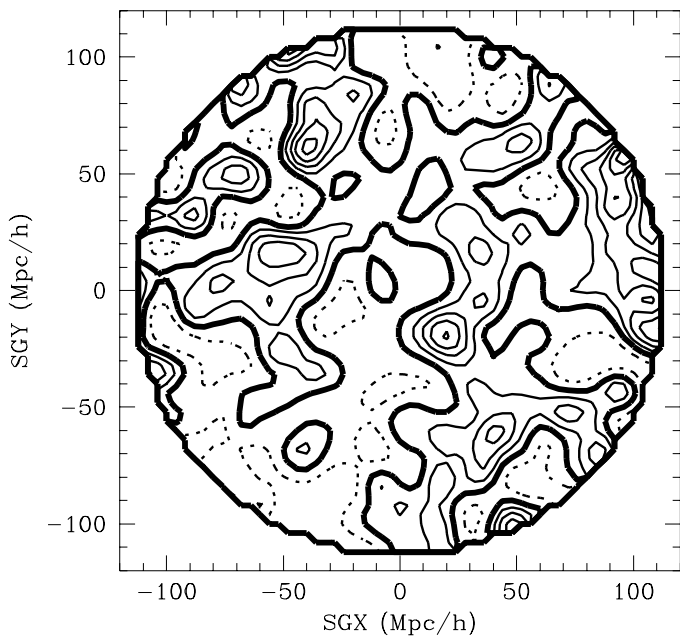
SGZ=+40



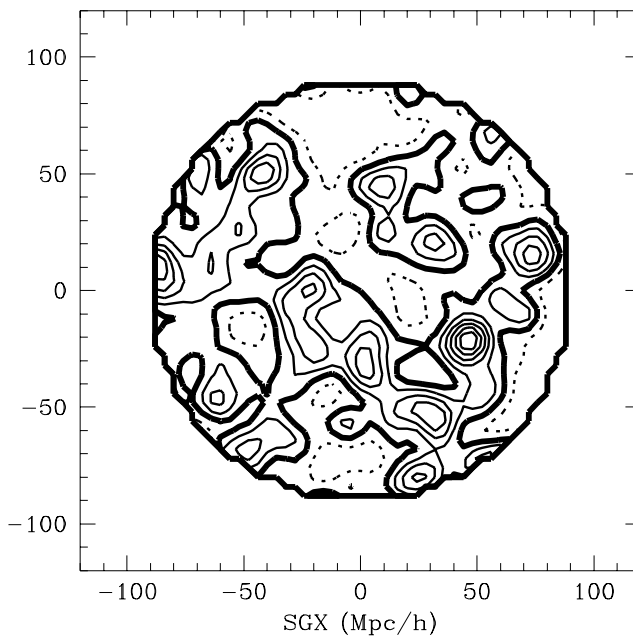
SGZ=+80



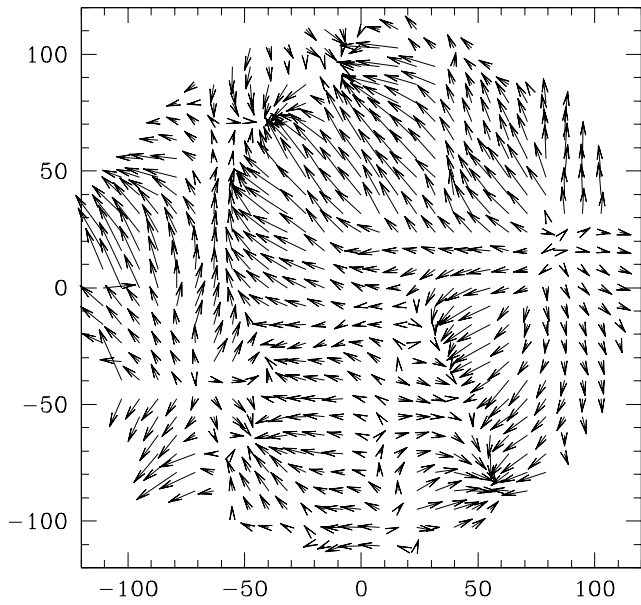
SGZ=-40



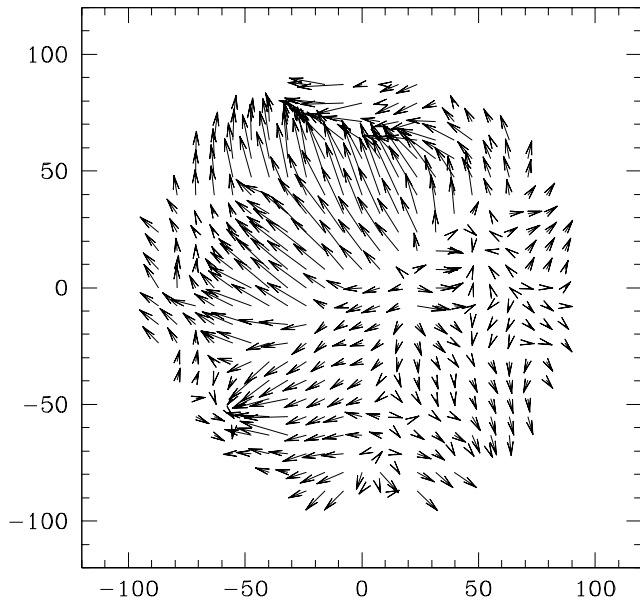
SGZ=-80



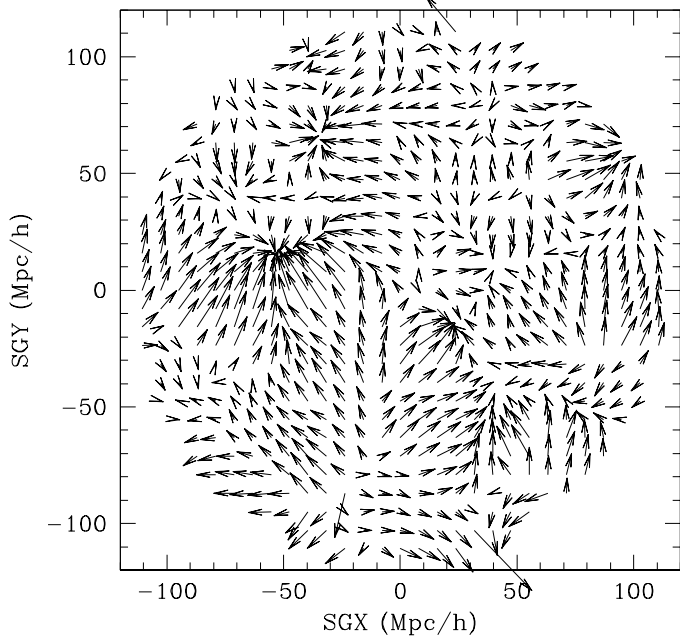
SGZ=+40



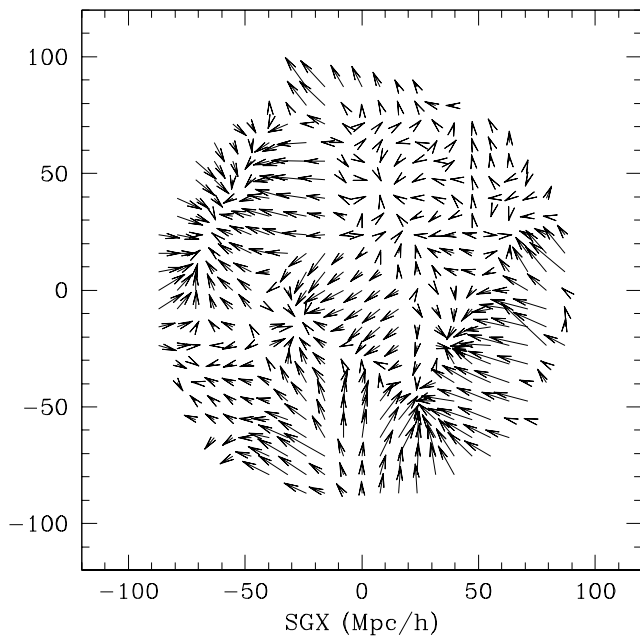
SGZ=+80

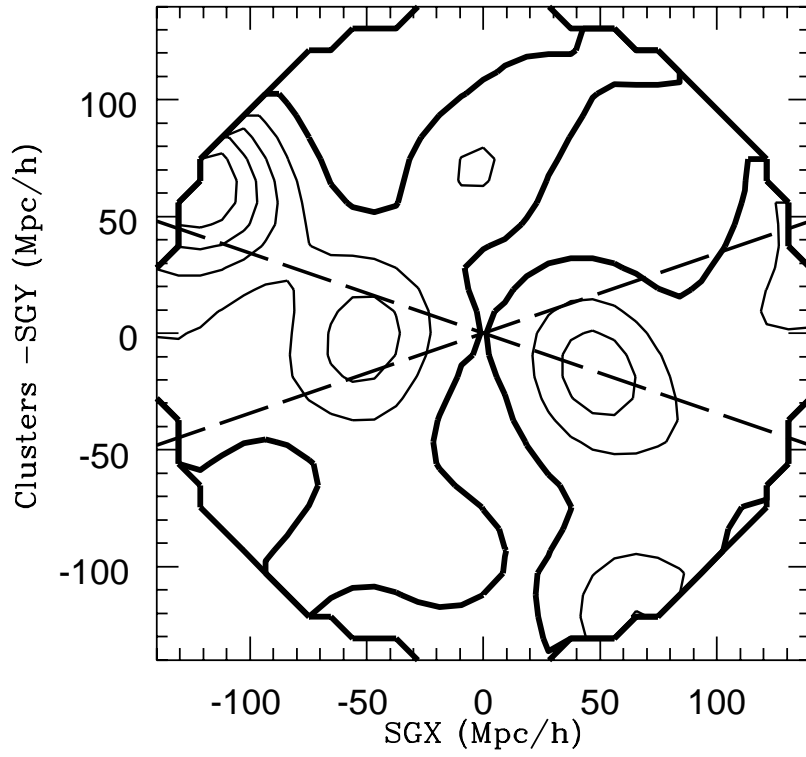
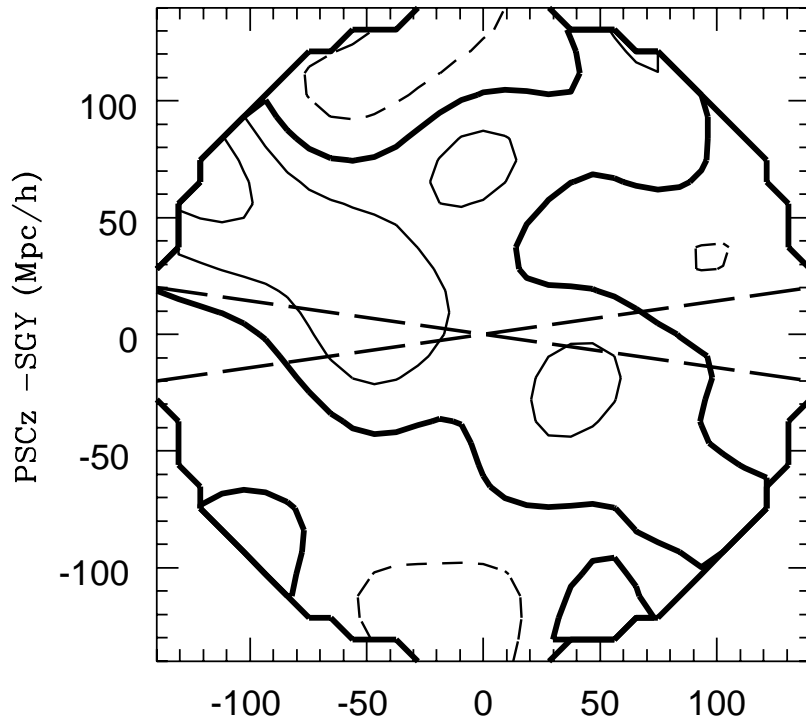


SGZ=-40

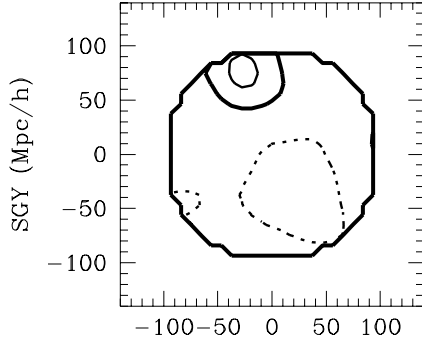


SGZ=-80

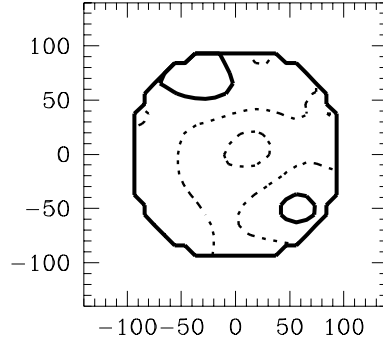




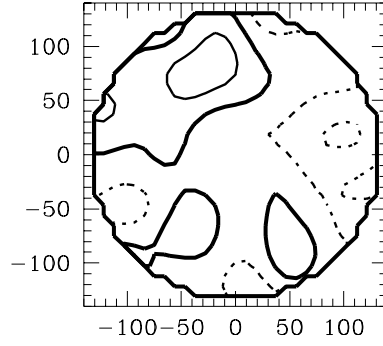
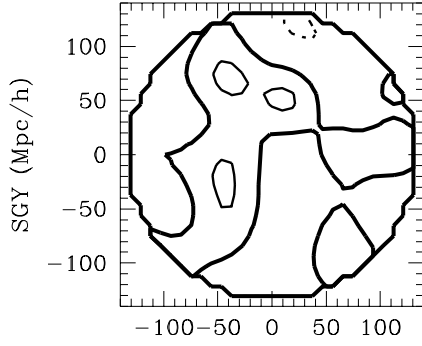
Abell/ACO Clusters



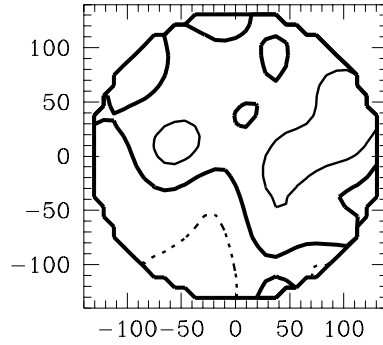
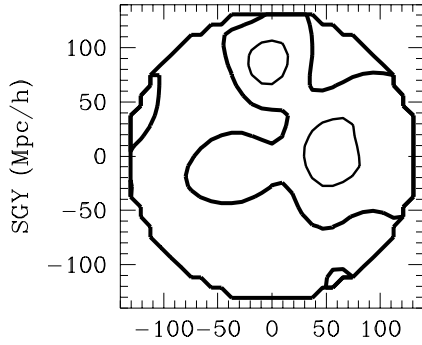
IRAS PSCz Galaxies



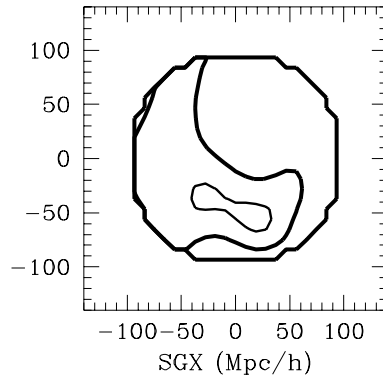
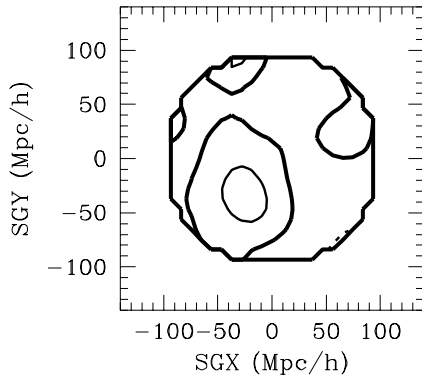
SGZ = +100 (Mpc/h)



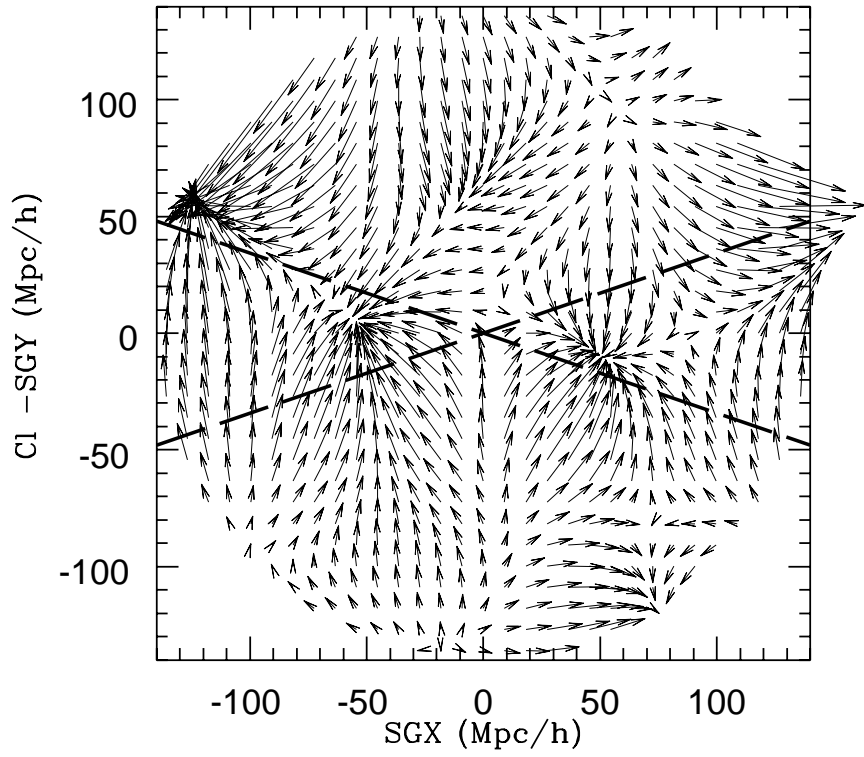
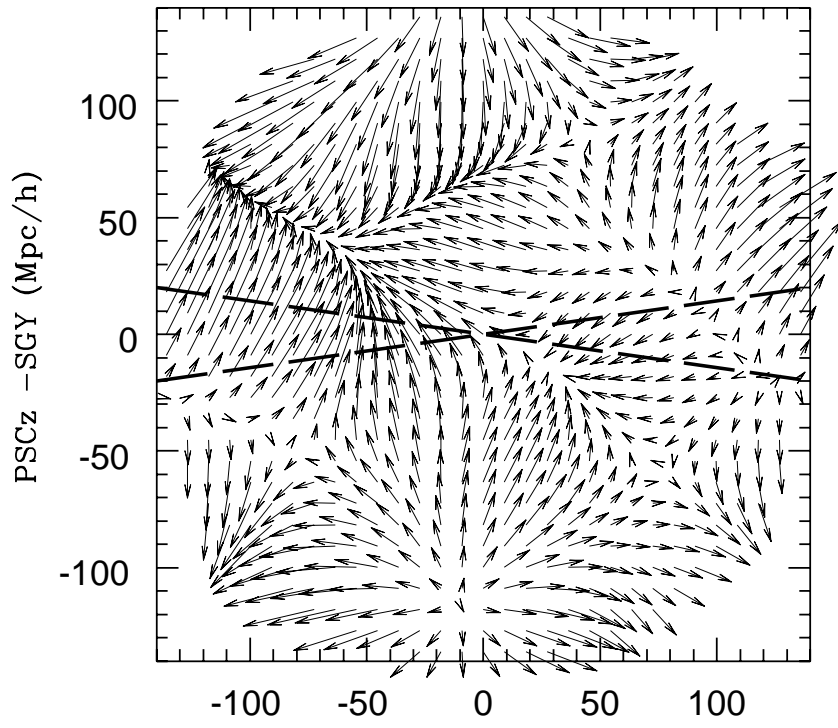
SGZ = +45 (Mpc/h)



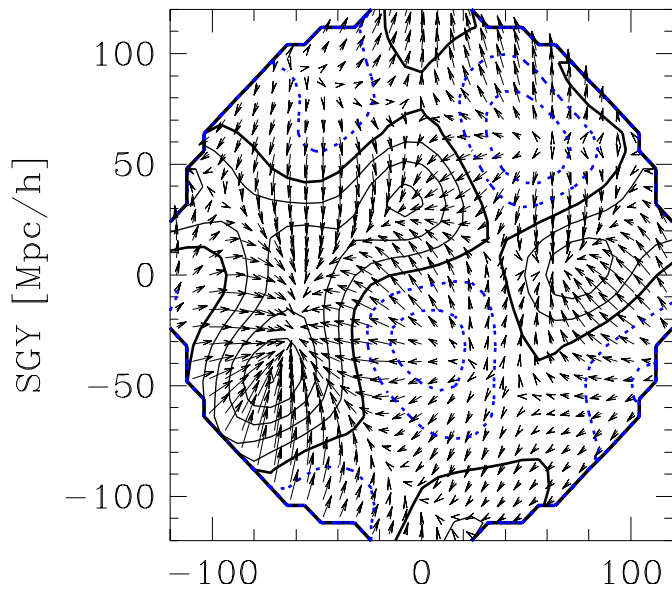
SGZ = -45 (Mpc/h)



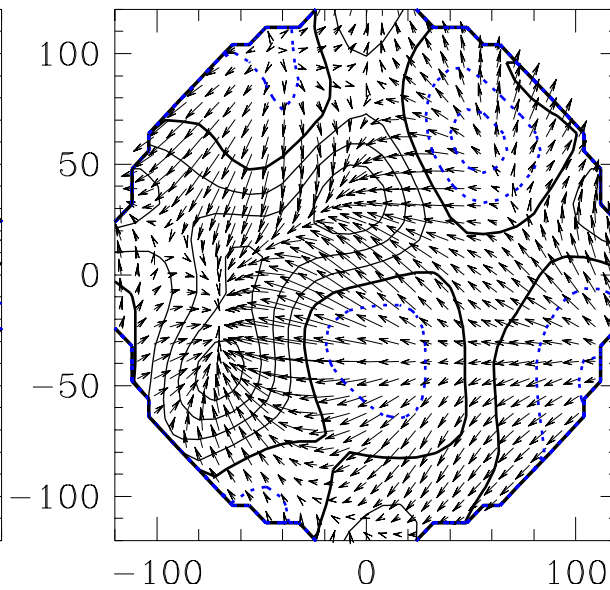
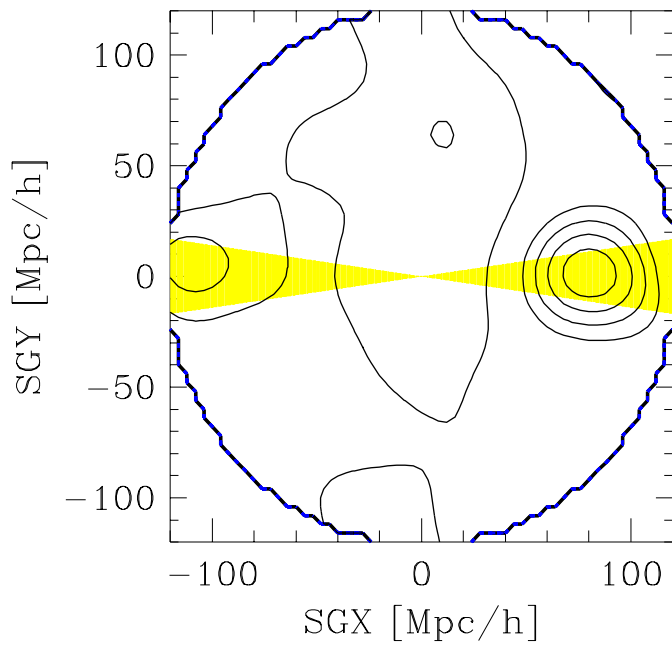
SGZ = -100 (Mpc/h)



TRUE



REC.

 $|\delta_{\text{TRUE}} - \delta_{\text{REC.}}|$  $v_{\text{TRUE}} - v_{\text{REC.}}$ 